Innovation and Sustainable Technology

3 papers

MACHINE LEARNING-ENABLED IOT ROBOTICS FOR PREDICTIVE MONITORING AND AUTONOMOUS CONTROL

Er. Ashutosh Karn[1], R. N. Thakur[2]

[1] Head of Incubation, Computer Science and Technology, LBEF College, Kathmandu, Nepal
[2] Professor, Computer Science and Technology, LBEF College, Kathmandu, Nepal

Abstract

Predictive maintenance increasingly combines machine learning (ML), Internet of Things (IoT) sensing, and robotics; however, the operational value of predictions is often evaluated less rigorously than predictive accuracy itself. This study investigates the transition from condition prediction to autonomous maintenance action through a four-layer framework comprising IoT sensing, edge prediction, a formal dispatch rule, and a capacity-limited maintenance robot. Five remaining useful life (RUL) models were evaluated on NASA C-MAPSS FD001 and FD003 across five random seeds, while five unsupervised anomaly detectors were evaluated over 34 experiments from the Skoltech Anomaly Benchmark (SKAB). Computational update cost was measured per model. Four maintenance policies ML-triggered, rule-based, hybrid, and fixed-interval were then compared using 100 run-to-failure trajectories, out-of-fold predictions, and 30 paired discrete-event simulation runs. Random Forest, XGBoost, LSTM, and CNN-LSTM showed no significant difference at the reported best RUL error levels, with best RMSE values of 11.99 and 12.65 cycles. Detector false-alarm rates ranged from 18% to 72%. At comparable unused asset life, ML-triggered dispatch reduced unplanned failures by 4.33 per 100 assets (95% CI [3.32, 5.34]) and reduced downtime by 21% relative to a sensor-threshold rule. The advantage increased with system load but disappeared when two robots were available. The findings show that predictive maintenance should be evaluated not only by prediction accuracy, but also by the timing and operational consequences of the maintenance actions initiated by those predictions.

Keywords: predictive maintenance, remaining useful life, anomaly detection, robotic maintenance dispatch, edge computing

INTRODUCTION

The industry 4.0 has helped the proliferation of sensing, connectivity, artificial intelligence and autonomous systems in industrial production and critical infrastructure. Predictive maintenance (PdM) is an emerging approach to implement along with the reactive and/or fixed interval maintenance, supported by the identification of the degradation in the functional state using condition data, and intervening before functional failure occurs. In industrial use, machine learning applications have been found in fault detection, fault diagnosis and remaining useful life estimation applications, and it has been observed that data quality, generalization, Interpretability & deployment are challenges (Carvalho et al., 2019; Theissler et al., 2021; Zonta et al., 2020). The current literature on prognostics and health management (PHM) also highlights the importance of health monitoring and life estimation as key inputs to predictive maintenance scheduling (Huang et al., 2024).

In PdM, there are two important analytical outputs: remaining useful life (RUL) and anomaly detection. The RUL is an estimate of the time or number of cycles until an asset exceeds a criterion. Anomaly detection, on the other hand, checks if there is any multivariate behaviour that is abnormal/unsuspecting from normal/expected behaviour. Neither the output is a

maintenance decision in itself, but they are both helpful. A RUL estimate of 20 cycles is not enough for a decision on intervention to be made now or later or based on further evidence. Likewise, the parameters to be considered for an anomaly alarm would be: persistence, severity, timing and the impact a false alarm would have on the cost. When resources for maintenance are limited, it matters a great deal whether it's prediction or action. For example, a mobile maintenance robot may not be able to maintain all the assets. In the case of a false alarm, the limited-service capacity could be used for no purpose, the maintenance could start too early, thereby wasting the useful life of the asset, or the service could be delayed, thereby leaving the asset to fail waiting in the queue. Wang et al. (2024) explicitly highlight the fact that many data-driven PHM studies focus on the prognostic aspect, and relatively few consider the following maintenance-decision problem. The correlation between the RUL information and maintenance scheduling has also been carried on recently and it highlights the criticality of the quality of the prediction and the quality of the actions (Walia & Kumar, 2026).

It is more complex to operate with Robotics. The feasibility of using data-driven models for fault diagnosis and remaining life estimation of robots has been shown by existing robotics-oriented PM research (Canizo et al., 2019). The complementary problem in the present study is to regard the robot as the maintenance resource which should be deployed according to the predicted information. The study therefore raises the question, whether there is a predictive signal that has a positive impact on maintenance outcomes under limited capacity of the robot.

The claim is for a system level benchmark and simulation framework, not for one single neural architecture. The study connects the concept of IoT sensing, edge prediction, dispatch rules presented as formal rules, and capacity-limited robotic execution, and validates these concepts through the use of public benchmark data sets and through discrete-event simulation. This shifts the focus of the assessment from “Which model predicts most accurately?” to “Which predictive information yields better maintenance decisions for realistic resources constraints?”

Research Questions

RQ1. What is the performance difference between representative machine-learning and deep-learning models in predicting the RUL for NASA C-MAPSS FD001 and FD003?

RQ2. What are the reliability properties of unsupervised anomaly detectors if false alarms are regarded as possible maintenance triggers?

RQ3. Could dispatching robots in response to the ML signal result in fewer unplanned failures and downtime than more basic rules-based maintenance policies, at equivalent unused asset life?

RQ4. What is the impact of availability of maintenance resources on the operational benefit of ML-triggered dispatch?

Research Objectives

- To benchmark five RUL models and five unsupervised anomaly detectors using established public datasets.
- To assess practical model update cost as an indicator of deployment feasibility.
- To compare ML-triggered, rule-based, hybrid, and fixed-interval dispatch policies using run-to-failure trajectories and discrete-event simulation.
- To evaluate operational outcomes in terms of unplanned failures, downtime, and unused asset life under different maintenance-capacity conditions.

LITERATURE REVIEW

Predictive Maintenance in Industry 4.0

Predictive maintenance has become a central research theme within smart manufacturing because connected sensors create continuous streams of operational data that can be processed using statistical and machine-learning methods. Carvalho et al. (2019) identified a wide range of ML approaches used in PdM and emphasized that algorithm selection must match the characteristics of the maintenance problem. Zonta et al. (2020) similarly highlighted the multidisciplinary nature of PdM in Industry 4.0 and the importance of integrating artificial intelligence, distributed computing, and engineering knowledge. Theissler et al. (2021) noted that data-driven PdM can benefit from multiple data sources but still faces challenges associated with labelled data availability, interpretability, and efficient deployment.

Remaining Useful Life and Prognostics

RUL prediction is a prognostic task in which the future time-to-failure or cycles-to-failure of an asset are estimated from condition information. PHM frameworks use RUL and other health indicators to support decisions about inspection, maintenance, and replacement (Huang et al., 2024). The NASA C-MAPSS turbofan degradation dataset is one of the most widely used benchmarks for this problem because it provides multiple multivariate run-to-failure trajectories under controlled combinations of operating conditions and fault modes (Saxena & Goebel, 2008; Saxena et al., 2008).

From Prognostic Accuracy to Maintenance Decisions

Prediction and maintenance planning are increasingly being studied together. Wang et al. (2024) state that most PHM studies focus on prognostic performance while relatively few address the maintenance-decision problem; their work links predicted RUL to dynamic maintenance decisions. Walia and Kumar (2026) likewise connect uncertainty-aware RUL estimation with maintenance scheduling in an industrial IoT context. These studies support a broader methodological argument: RUL is valuable when it improves maintenance decisions, not simply when it reduces an error metric.

Robotics and Predictive Maintenance

Robotics-oriented predictive maintenance has traditionally focused on predicting faults of the robot itself. Canizo et al. (2019), for example, demonstrated a data-driven methodology for robot fault detection and remaining-life estimation. The present research extends the relationship between robotics and PdM in a different direction by treating the robot as the maintenance executor. This requires the predictive signal to be converted into a dispatch rule and evaluated under queueing and capacity constraints.

MATERIALS AND METHODS

Research Design

This study used a quantitative benchmark-and-simulation research design. It did not involve human participants, interviews, questionnaires, animals, or personal data. Secondary engineering time-series data were obtained from public benchmark repositories. The study proceeded from data acquisition and model benchmarking to policy-level discrete-event simulation so that

predictive performance and maintenance outcomes could be evaluated separately and then linked.

The experimental protocol had four main components:

(1) Benchmark five RUL models on C-MAPSS FD001 and FD003 across five random seeds; benchmark five unsupervised anomaly detectors over 34 SKAB experiments

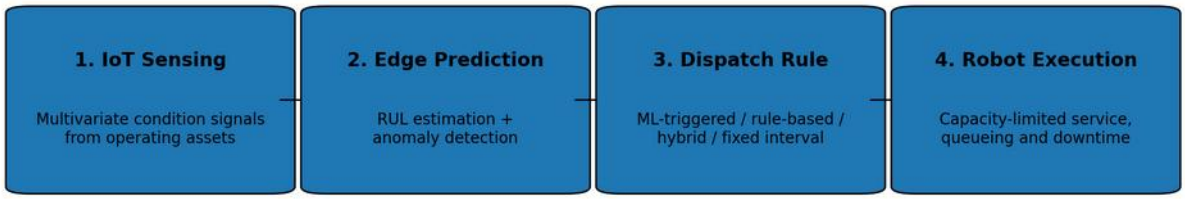
(2) Measure model computation time per update; and

(3) Evaluate four robot-dispatch policies over 100 run-to-failure trajectories using out-of-fold predictive signals and 30 paired discrete-event simulation runs.

Conceptual Four-Layer Architecture

The proposed framework contains four layers that convert condition information into maintenance execution.

Figure 1*: Summarizes the architecture*



The proposed framework consists of four interconnected layers that link predictive analytics with robotic maintenance action. The first layer, IoT Sensing, collects multivariate condition data such as temperature, pressure, vibration, electrical current, and other health indicators, represented in this study by the C-MAPSS and SKAB datasets. The second layer, Edge Prediction, processes these signals to estimate the asset condition through Remaining Useful Life (RUL) prediction or anomaly detection; although the concept assumes near-equipment inference, the reported timing measurements were obtained on a server CPU rather than embedded edge hardware. The third layer, Formal Dispatch Rule, converts the predictive or sensor-based information into a maintenance decision using ML-triggered, sensor-threshold, hybrid, or fixed-interval policies. Finally, the Capacity-Limited Robot Execution layer models a maintenance robot with finite service capacity, allowing requests to queue when the robot is busy. This four-layer design enables the study to evaluate not only prediction performance but also how effectively predictive information improves the timing and operational value of robotic maintenance.

Data Collection Method

Part of the study was conducted through secondary quantitative data from the existing open engineering benchmark datasets and not by gathering data from a physical maintenance robot. C-MAPSS was chosen as the run-to-failure degradation trajectories for supervised Remaining Useful Life (RUL) prediction, and SKAB was chosen as the industrial testbed signals with multivariate anomalies for the unsupervised anomaly detection evaluation. The data flow for data processing included data acquisition, integrity and structure validation, chronological data organization, label/target preparation, data preprocessing, model training or anomaly scoring, data prediction, model performance evaluation, and data dispatch simulation. Using public benchmark datasets can enhance the ability to be reproducible and to compare with previous

studies, but the uncertainties in the environment, mechanics, communication and maintenance of real-world industrial deployments cannot be fully captured in benchmark datasets.

NASA C-MAPSS Dataset

C-MAPSS (Commercial Modular Aero-Propulsion System Simulation), is a NASA benchmark using multivariate run to failure turbofan engine degradation data under various operating conditions and fault modes (Saxena & Goebel, 2008). Each engine is modeled as a time series of operating settings and sensor measurements taken over successive operating cycles. Remaining Useful Life (RUL) is defined as the number of cycles remaining until an engine fails, $RUL_i(t) = T_i - t$, T_i is the number of the final failure cycle, and (t) is the number of the current operating cycle. If the RUL of an engine is 40 cycles, but it fails at cycle 220 and is observed at cycle 180, the observed RUL is 40 cycles. The predictive model is thus based on current and past sensor performance to predict the engine's remaining usable life.

Table 1

C-MAPSS subsets used in the study

Subset	Training engines	Test engines	Operating conditions	Fault modes
FD001	100	100	1	1 (HPC degradation)
FD003	100	100	1	2 (HPC and fan degradation)

Note. Subset characteristics are consistent with the standard C-MAPSS benchmark documentation and commonly reported dataset descriptions (Saxena & Goebel, 2008; Saxena et al., 2008).

Multivariate Time-Series Structure and Preprocessing

In C-MAPSS, multivariate time-series data are collected at consecutive engine cycles with several sensor measurements and operating conditions, to account for the combined effect of degradation over time. The data are grouped chronologically by engine, RUL targets are created for the final failure cycle, certain sensor channels that do not provide informative data are filtered out, and numerical features are scaled to perform normalization. One of the most popular ways of standardizing is the z-score transformation, and it is often used in practice.

$z = (x - \mu) / \sigma$, where (x) is the observed value, (μ) is the mean of the training-features and (σ) is the standard deviation of the training-features. In case of temporal models, like LSTM and CNN-LSTM, the sequences of the sensor observations can be arranged into sliding windows to forecast the RUL at the current cycle as well. The specific feature-selection method, scaling parameters, RUL-capping rule and sequence length should be reported based on the original experimental data, instead of being deduced from the conference abstract or presentation.

Skoltech Anomaly Benchmark (SKAB)

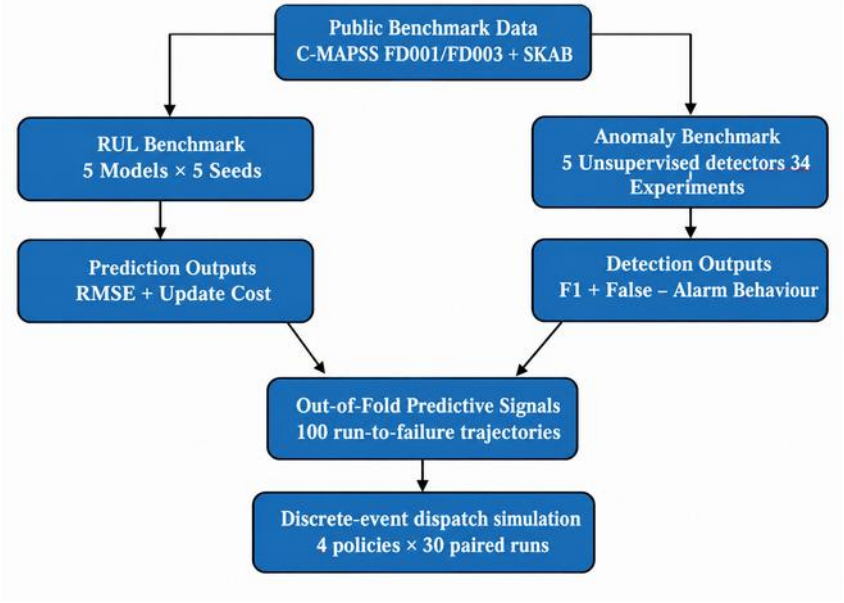
For the evaluation of the reliability of the anomaly detection, multivariate time-series data gathered from an industrial testbed such as vibration, motor current, pressure, temperature, voltage and flow related measurements were used (Katser & Kozitsin, 2020). We used five unsupervised anomaly detectors in 34 experiments. Unsupervised detection: In this case, the model learns to detect observations or sequences of observations that are abnormal or atypical

from an operating behavior, without the need for a large number of labelled examples of faults. The typical output from each detector is an anomaly score, which is then compared with a criterion value to determine if an observation is normal or abnormal. The selection of the threshold is thus an important step since higher sensitivity can help detect faults, but may also lead to more false alarms, which has a direct impact on the maintenance decision.

Discrete-Event Simulation

The four maintenance policies were evaluated using 100 run-to-failure trajectories and 30 paired discrete-event simulation runs, where the system was modelled as a sequence of time-ordered events including degradation updates, maintenance requests, robot dispatch, queueing, service initiation, service completion, and failure. This approach is appropriate because both event timing and limited-service capacity determine whether maintenance can be completed before an asset fails. Paired simulation runs allowed alternative policies to be compared under matched conditions, reducing the influence of unrelated scenario variation. Performance was assessed using unplanned failures, downtime, and unused asset life, with unused asset life acting as an important balance against excessively early maintenance. Sensitivity analysis was also conducted for system load and robot capacity to determine whether policy performance depended on resource scarcity and queueing conditions.

Figure 2: *Evaluation workflow linking public benchmarks to maintenance-dispatch simulation*



RESULTS AND DISCUSSION

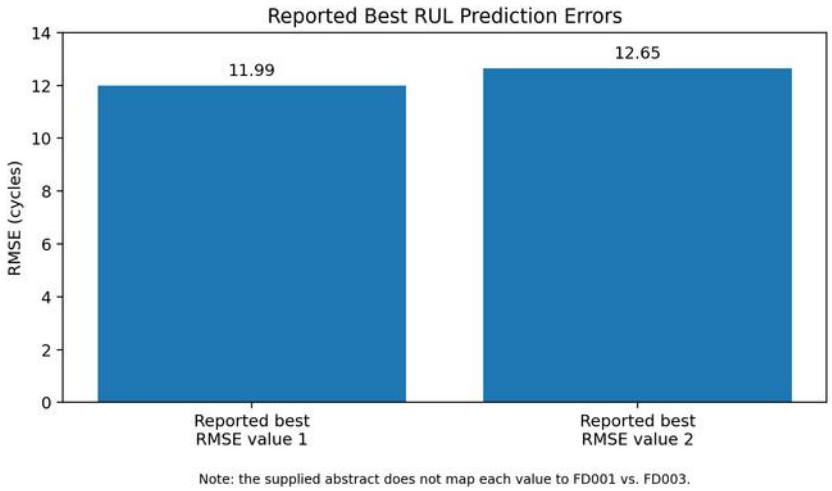
Result 1: RUL Prediction Performance

There was no clear dominance of any one reported model family from the RUL benchmark. Random Forest (RM) and XGBoost (XGB) were reported as giving the same best RMSE, 11.99 and 12.65 cycles respectively, in the C-MAPSS FD001 and FD003 experiments, and LSTM and CNN-LSTM reported no statistically significant difference at the best RMSE. In the supplied abstract it is not specified which numerical value should refer to which subset, so the present

paper does not make any attempt to assign the two values to either FD001 or FD003, but rather deliberately avoids doing so without the original experiment log.

The errors reported for the two best trials are 0.66 cycles apart in absolute value. This is not a model-to-model effect, as the values are the sum of two benchmark conditions, and not a complete per-model result table. The defensible conclusion that can be drawn from the study is that the "biggest" model families were not statistically different when compared against the specific benchmark. Practical criteria like latency, memory requirement, stability across seeds and interpretability of the model, ease of edge deployment should also be taken into account when making the model selection.

Figure 3: Reported best RUL prediction errors

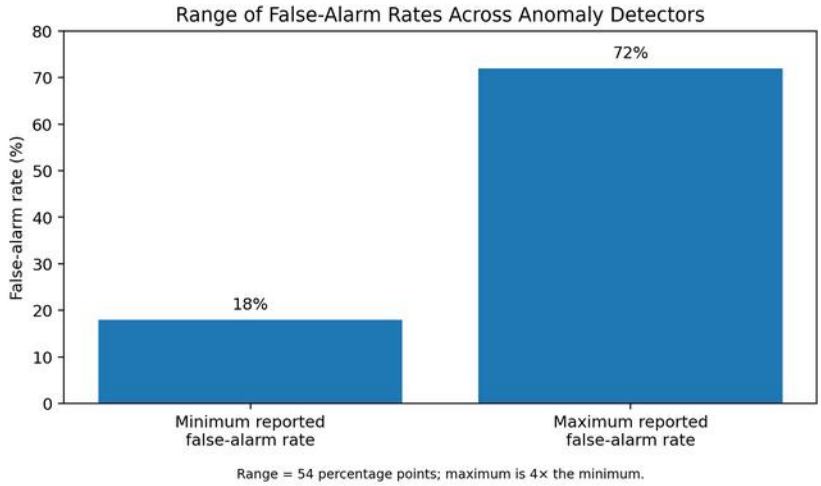


Result 2: Anomaly Detection Reliability

The RUL results were significantly more stable than the results in the anomaly detection. The false alarm rates of the 5 unsupervised detectors were between 18% and 72%, representing a difference of 54 percentage points. The false alarm rates of the 34 SKAB experiments were between 18% and 72% (54 percentage points apart). The highest false alarm rate reported is four times the lowest. This is a large dispersion, which suggests that the choice of detector and alarm logic is a policy critical issue – an algorithm that seems quite good on the basis of an aggregate score can have a very different maintenance burden when it translates to robotic actions.

The second portion of the abstract reads further that most of the false alarms were after the onset of the event and that one detector flagged all the points at F1 = .703. This is a significant methodological caveat. To reach a strong recall value, yet still return to a seemingly reasonable F1 value, a detector which returns a fault across several time points can return a fault for the whole post-fault region. Event metrics like first-detection delay, alarms per fault event, pre-fault false alarms, duplicate-alarm rate and time-to-action, therefore, provide more information as complementary measures to point-wise F1 for autonomous maintenance.

Figure 4: *Range of reported anomaly-detector false-alarm rates*



Result 3: Computational Update Cost

It claimed to achieve less than 0.5ms per update computational latency for all models tested (excluding Random Forest) on a server CPU with 32-bit precision. This result would aid fast inference in the tested server environment and it seemed that the latency for prediction was not the most critical constraint in the simulation. It can't define performance for embedded edge hardware, however. In addition to CPU model, number of threads, batch size, warm-up procedure, number of timing repetitions, memory footprint and energy consumption, the deployment study for a publication should also contain energy consumption.

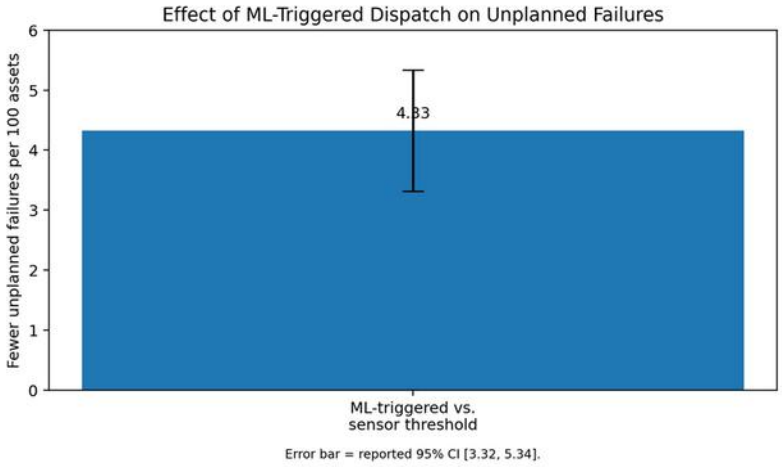
Result 4: ML-Triggered Dispatch and Unplanned Failures

For the same amount of unused asset life, the ML-triggered dispatch approach resulted in significant reductions in unplanned failures for 4.33 per 100 assets, compared to the sensor-threshold approach. The reported 95% confidence interval was of width 2.02 failures per 100 assets and half-width about 1.01 around the point estimate, [3.32, 5.34]. For the experiment described, the paired simulation result is positive and the entire interval is positive, which suggests that for this experiment, the reduction in failures is positive. P-value should NOT be generated when the inferential test is not provided in the materials specified.

The phrases “for the same amount of unused asset life” are of analytical importance. It is not only that he is doing maintenance earlier and discarding more remaining life, it's that he is doing maintenance earlier and discarding more remaining life than the failure reduction number implies. In the end, however, it seems ML was equally conservative when it comes to dispatching.

Result 5: Downtime Reduction

Figure 5: *Reduction in unplanned failures with ML-triggered dispatch*



The per-update computational latency was claimed to be less than 0.5ms for all models tested except Random Forest when using 32-bit precision on a server CPU. This result would aid fast inference in the tested server environment and it seemed that the latency for prediction was not the most critical constraint in the simulation. It can't define performance for embedded edge hardware, however. The deployment study for a publication should also include CPU model, number of threads, batch size, warm-up procedure, number of timing repetitions, memory footprint, and energy consumption.

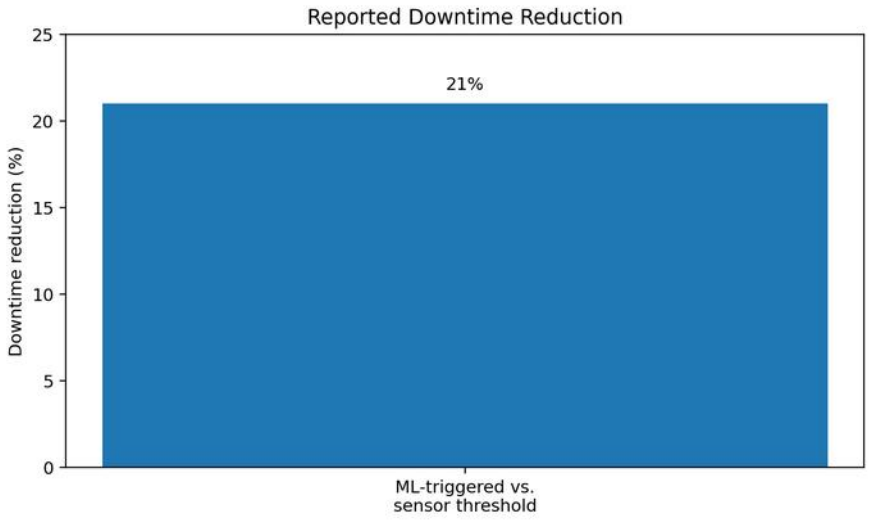
Result 4: ML-Triggered Dispatch and Unplanned Failures

The ML-triggered dispatch approach significantly curtailed unplanned failures at 4.33 per 100 assets compared to the sensor-threshold approach, for the same amount of unused asset life. The reported 95% confidence interval was [3.32, 5.34] with a width of 2.02 failures per 100 assets and a half-width of about 1.01 around the point estimate. The entire reported interval is greater than zero, indicating that, for the experiment described, the paired simulation result is consistent with a positive reduction in failures. You should not create a p-value where the specified inferential test is not given in the provided materials.

The terms “for the same amount of unused asset life” are of analytical significance. It does not just mean that he's doing maintenance earlier and discarding more remaining life; it means that he's doing maintenance earlier and discarding more remaining life than the failure reduction number suggests. However, the outcome suggests that ML achieved a similar degree of conservativeness in its dispatch timing.

Result 5: Downtime Reduction

Figure 5: *Reduction in unplanned failures with ML-triggered dispatch*



The dispatch system, activated by the ML, reduced downtime by 21% when compared with the sensor-threshold rule. This is a more robust indicator than prediction error, since downtime directly translates to the time that assets are idle or not productive. There was no base line downtime value provided therefore, it is impossible to measure a time saving without the original simulation output. As per, the result should be reported as a relative 21% reduction and NOT as hours or cycles.

Result 6: System Load and Robot Capacity

The benefit of the dispatch by ML decreased as the number of robots increased to two, and increased as the load increased. This is one of the most important results of the study, because it indicates how the benefit is being achieved. When there is a limited resource that needs to be allocated to maintenance requests, the time of dispatch and prioritization is important, especially when there is only one robot available. If a second robot is added on, queueing pressure is reduced and easier policies will be able to meet the demand of the queue in a timely manner that the ‘incremental advantage’ of ML timing is moot.

So, a general rule of ML-induced maintenance is not possible. It allows for a conditional statement: ML-triggered dispatch is best used in systems with limited capacity where bad time can directly lead to queueing delay, failure and downtime.

Figure 6: *Reported downtime reduction under ML-triggered dispatch*

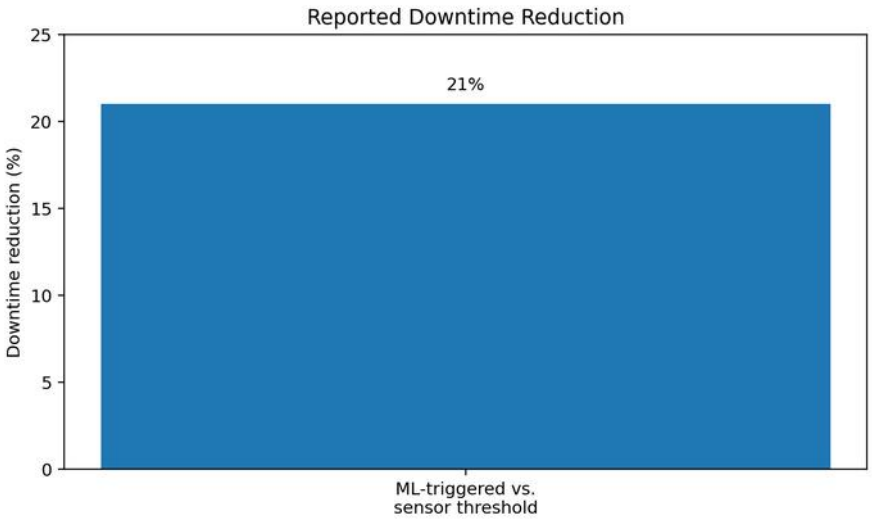


Table 4

Summary of principal study findings

Evaluation component	Reported finding	Engineering interpretation
RUL prediction	Best RMSE values 11.99 and 12.65 cycles; no significant difference among the leading reported model families.	Accuracy alone does not justify additional model complexity.
Anomaly detection	False-alarm rates ranged from 18%-72% false-alarm range; F1 = .703 for a broadly flagging detector	Prediction was fast in the tested environment; embedded performance remains unverified.
Unplanned Failures	<0.5 ms for all models except 4.33 fewer per 100 assets; 95% CI [3.32, 5.34]	Positive effect under the paired simulation protocol, with uncertainty quantified.
ML-triggered dispatch	4.33 fewer unplanned failures per 100 assets; 95% CI [3.32, 5.34].	Prediction improved maintenance timing at comparable unused life.
Downtime	21% reduction relative to sensor-threshold policy.	Better timing produced a system-level benefit.
Load/Capacity sensitivity	Benefit increased with load and disappeared with two robots.	Resource scarcity determines the value of intelligent dispatch.

Discussion

The results confirm the transition from model-based to decision-based predictive maintenance, and the role of machine learning is not only demonstrated in terms of prediction but also in terms of improving maintenance activities. While the RMSE were statistically equivalent between the leading RUL models, the false alarms in the anomaly detectors revealed a significant spread, indicating that models with similar technical performance can still be seen to be operationally sub-optimal. In the case of robotic maintenance, this is particularly crucial as it can cause unnecessary physical movements, rack up the robot's time, energy, tools, and queue capacity, and postpone real maintenance requests. The findings of the ML-triggered dispatch policy were clear, with the reduction of unplanned failures per 100 assets by 4.33 and downtime by 21%. This has not been about predicting failures, but rather about the timing of interventions. This benefit was heavily dependent on system capacity however, as under higher load conditions it was evident, but not present when the load was two robot(s) and maintenance resources were two, indicating that intelligent dispatch is most useful when maintenance is limited. The results

also indicate that the capability to predict and prioritize should be considered with capacity, and that the cost of extra robots vs. the benefit of better prediction and prioritization should be taken into account. In terms of edge-AI, the sub-millisecond inference time on the server-CPU is a sign of computational feasibility, but the deployment in the embedded system still needs to be tested within memory, power, communications, synchronization, and hardware constraints. In general, the study has strengthened the case for using operational measures (e.g., the reduction of failures, downtime, timing of alarms, utilisation of resources and capacity limitations) over traditional measures (e.g., RMSE, F1) when assessing the usefulness of predictive-maintenance systems. To ensure better reproducibility and independent verification for publication-grade reporting, more detailed per-model, per-detector and per-simulation statistics should be provided.

Limitations

The study is limited as it depends on the public benchmark datasets, and on the use of discrete-event simulation instead of the deployment of physical maintenance robots. C-MAPSS and SKAB are controlled and reproducible datasets for assessing RUL prediction and anomaly detection; however, the datasets can never fully represent the variations of real industrial environments, factories, infrastructure systems, and robotic platforms. These latency, memory, thermal and power consumption figures are from a server CPU and may vary on embedded edge devices and robot controllers which operate in 32-bit precision mode. Also, several details that are critical for reproducibility, such as the fifth RUL model, the names of the anomaly detectors, exact hyperparameters, preprocessing settings, anomaly thresholds, and inferential test are not stated in the provided abstract and presentation and should be obtained from the original experiment scripts prior to final publication. Lastly, the simulation models did not capture the full range of practical considerations, including navigation, avoidance of obstacles, battery management, tool changes, communication failures, uncertainty in repairs, safety considerations, and human-robot interaction, which can all impact the scalability of the robot.

Conclusion

In this study, a four-layer architecture that covers IoT sensing, edge-side prediction, formal maintenance dispatch, and capacity-limited robot execution is proposed to analyze the full process of prediction-to-action in the PM system. At the best RMSE, there was no evident preference among the three models Random Forest, XGBoost, LSTM and CNN-LSTM for the RUL benchmark, and anomaly detection yielded false alarm rates between 18% to 72% indicating that good predictive performance does not necessarily lead to good maintenance decisions. Most significantly, the ML-driven dispatch reduced unplanned failures by 4.33 per 100 assets and downtime by 21% while compared to a sensor-threshold policy at a similar unused asset life. This benefit was most pronounced when there was limited capacity for maintenance, however, and vanished when two robots were available, indicating that there is a critical resource capacity constraint. The study suggests that instead of using the prediction metrics themselves, the effectiveness of a predictive-maintenance system should be judged through its contribution to quality and operational impact of the maintenance actions it allows. Future work should test the framework on embedded edge computing devices and physical robots and consider the inclusion of energy, cost, safety, uncertainty-aware dispatch, duplicate alarm control, and multi asset and multi robot configurations.

Acknowledgments

The authors acknowledge LBEF College, Kathmandu, Nepal, for the academic environment associated with this research. Any additional institutional, laboratory, technical, or project acknowledgments should be inserted only if they accurately reflect the support received.

Funding

Funding information was not provided in the supplied research materials and should be confirmed by the authors before submission. If no external funding was received, the NCET template permits the statement: “The authors received no financial support for the research, authorship, or publication of this paper.”

Conflict Of Interest

The conflict-of-interest declaration should be confirmed by the authors before submission. If no conflict exists, the statement may read: “The authors declare no conflict of interest.”

Author Contributions

A final contribution statement should be confirmed by both authors. Based on the supplied materials, a proposed formulation is **Er. Ashutosh Karn** conceptualization, methodology, analysis, investigation, visualization, writing original draft, and presentation; Prof. Dr. R. N. Thakur supervision, methodological guidance, validation, and writing review and editing. This statement must be verified before publication.

Data Availability

The NASA C-MAPSS turbofan engine degradation dataset is publicly available through the NASA Prognostics Center of Excellence repository. The Skoltech Anomaly Benchmark is publicly available through its benchmark repository/Kaggle DOI. Availability of the study-specific code, trained models, simulation configuration, and experiment logs should be stated by the authors at submission.

Ethical Approval / Consent

Not applicable. The study used public engineering benchmark datasets and simulation and did not involve human participants, animals, or identifiable personal data.

References

Breiman, L. (2001). Random forests. *Machine Learning, 45, 5–32.*

Canizo, M., Onieva, E., Conde, A., Charramendieta, S., & Trujillo, S. (2019). *Robot fault detection and remaining life estimation for predictive maintenance. Procedia Computer Science, 151, 709–716. https://doi.org/10.1016/j.procs.2019.04.094*

Carvalho, T. P., Soares, F. A. A. M. N., Vita, R., Francisco, R. da P., Basto, J. P., & Alcalá, S. G. S. (2019). *A systematic literature review of machine learning methods applied to predictive maintenance. Computers & Industrial Engineering, 137, 106024. https://doi.org/10.1016/j.cie.2019.106024*

Chen, T., & Guestrin, C. (2016). XGBoost: *A scalable tree boosting system. In Proceedings of the 22nd ACM SIGKDD International Conference on Knowledge Discovery and Data Mining (pp. 785–794). Association for Computing Machinery. https://doi.org/10.1145/2939672.2939785*

Hochreiter, S., & Schmidhuber, J. (1997). *Long short-term memory. Neural Computation, 9(8), 1735–1780. https://doi.org/10.1162/neco.1997.9.8.1735*

Huang, C., Bu, S., Lee, H. H., Chan, C. H., Kong, S. W., & Yung, W. K. C. (2024). *Prognostics and health management for predictive maintenance: A review. Journal of Manufacturing Systems*, 75, 78–101. https://doi.org/10.1016/j.jmsy.2024.05.021

Katser, I. D., & Kozitsin, V. O. (2020). *Skoltech Anomaly Benchmark (SKAB).* Kaggle. https://doi.org/10.34740/KAGGLE/DSV/1693952

Saxena, A., & Goebel, K. (2008). *Turbofan engine degradation simulation data set. NASA Ames Prognostics Data Repository, NASA Ames Research Center.*

Saxena, A., Goebel, K., Simon, D., & Eklund, N. (2008). *Damage propagation modeling for aircraft engine run-to-failure simulation. In 2008 International Conference on Prognostics and Health Management (pp. 1–9). IEEE*.

Theissler, A., Pérez-Velázquez, J., *Kettelgerdes, M., & Elger, G. (2021). Predictive maintenance enabled by machine learning: Use cases and challenges in the automotive industry. Reliability Engineering & System Safety, 215, 107864.*

Walia, G. K., & Kumar, M. (2026). Uncertainty-aware remaining useful life prediction and PPO based optimal maintenance scheduling in industrial IoT. Reliability Engineering & System Safety, 273, 112356.

Wang, L., Zhu, Z., & Zhao, X. (2024). *Dynamic predictive maintenance strategy for system remaining useful life prediction via deep learning ensemble method. Reliability Engineering & System Safety, 245, 110012.*

Zonta, T., da Costa, C. A., da Rosa Righi, R., de Lima, M. J., da Trindade, E. S., & Li, G. P. (2020). *Predictive maintenance in the industry 4.0: A systematic literature review. Computers & Industrial Engineering, 150, 106889.*

Mechanical Performance of Natural Fiber Reinforced Polymer Composites: A Study on Agave Fiber and Recycled LDPE

R. M. Lamichhane [1], S.P. Adhikari [2*],

[1]Department of Automobile and Mechanical Engineering, Thapathali Campus, Institute of Engineering, Tribhuvan University, Nepal

[2] Department of Mechanical and Aerospace Engineering, Pulchowk Campus, Institute of Engineering, Tribhuvan University, Nepal

[1] ram.080msedm09@tcioe.edu.np

[*] surya@tcioe.edu.np / 0000-0001-9527-4650

Abstract

The growing global reliance on plastics, especially in agriculture and food packaging, has raised serious environmental and public health concerns, as most plastic waste is discarded rather than reused, recycled or incinerating. Natural fibers are gaining importance owing to their low weight, cost-effectiveness, environmental friendliness, and sustainability. This research investigates the fabrication and mechanical performance of natural fiber reinforced polymer composites (NFRPC) made from agave fiber and recycled low density polyethylene (LDPE). Fibers were extracted from fresh agave leaves by an underground retting process for 30 days, then cleaned and dried before treatment. Short fibers, treated with 6% (w/v) NaOH solution were used at 0, 5, 10, 15 and 20 wt.%, while a composite with 15 wt.% untreated fiber was produced for comparison. The fibers were mixed with recycled LDPE and fed into a single screw extruder at 165 °C. The specimens' tensile and compressive test was conducted. Tensile strength and compressive strength of the composite was found at 19.10 Mega pascals (MPa) and 19 MPa, respectively, for 15 wt.% of treated fiber loading, which was 12.40 MPa and 11MPa for untreated fiber. Both Ultimate strength in tension and compression were maximum at 15 wt.% loading of NaOH treated fiber. This improvement is attributed to the alkaline treatment, which enhances fiber and matrix adhesion and load transfer. The findings show that alkali-treated agave fiber can effectively reinforce recycled LDPE, giving a sustainable composite suitable for lightweight engineering applications.

Keywords: agave fiber, recycled LDPE, composite, tensile strength, compressive strength.

1. Introduction

The widespread application of plastics across diverse sectors has led to the current era being characterized as the "plastic age” Strikingly, nearly 50% of total plastic production to date has occurred in just the last 15 years (Dokl et al., 2024). Projections indicate that plastic waste in the environment could reach 5.3 gigatons by 2050. More than 90% of it is released without any prior treatment and ends up in oceans and landfills, which poses a serious risk to ecosystems and human health(Mendoza et al., 2024). Because the majority of plastics particularly those derived from petroleum don't break down easily, they can remain in the environment for anywhere from fifty years to a thousand years, causing harmful consequences for ecosystems(Macheca et al., 2024). Bioplastics emit less carbon than conventional plastics and can be recycled repeatedly, helping balance the environmental carbon cycle. Global bioplastic capacity, about 2.47 million tons in 2024 ,56.3% biodegradable, is projected to reach 5.73 million tons by 2029, with the biodegradable share rising to 66%(Huang et al., 2025).

Plastic recycling covers the whole process of collecting plastic waste and reprocessing it into new products, either mechanically, which preserves the original chemical structure, or chemically, which alters the composition. Polyethylene (PE) is the most valuable and widely recycled post-consumer plastic worldwide(Singh & Walker, 2024) . Recycling thermoset composite waste is both economical and environmentally beneficial, it avoids the high energy and cost of producing new fibers, prevents pollution from landfilling, and extends the service life of high-value fibers (Utekar et al., 2021). Sustainable bio-composites are gaining ground as an alternative to conventional plastics, with recycled polymers helping cut virgin plastic use and repurpose waste(Ali et al., 2026) . Composites formed by combining natural fibers with bio-based polymers are known as green composites. Common natural fibers used include coir, flax, sisal, and hemp, while examples of bio-polymers include starch, polylactic acid (PLA), cashew nut shell liquid (CNSL), and furan (Shekar & Ramachandra, 2018). Natural fiber reinforced polymer composites (NFPCs) are made from renewable resources, offer environmental benefits, and sequester carbon, while meeting industrial needs. They combine natural fibers with either petroleum based or bio- based polymers (Ramachandran et al., 2022).

A sustainable circular plastics economy requires halving future plastic demand, phasing out fossil-derived plastics, recycling 95% of retrievable plastics, and adopting renewable energy, supported by redesign, alternative materials, reduced virgin plastic use, and reuse.(Singh & Walker, 2024).

Natural organic fibers have been widely recognized as eco-friendly reinforcements for polymer composites. Combining agave fiber with different polymers offers a sustainable option for non-structural or semi-structural applications. Despite this potential, the properties of composites produced by incorporating short agave fiber into recycled LDPE remain insufficiently explored, particularly regarding lowering carbon emissions, waste management and environmental burden, as well as their mechanical behavior and the interfacial adhesion between the matrix and short agave fibers. This study, therefore, examines the mechanical properties of recycled LDPE composites reinforced with short fiber from *Agave americana*, locally known in Nepal as Ketuki, Specifically, the effects of fiber loading (0–20 wt.%) and NaOH treatment on the tensile and compressive strength of the composites are evaluated, supported by SEM analysis, in this research. This work contributes to The United Nations, Sustainable Development Goal “SDG12” by promoting renewable, low-waste composite materials as sustainable alternatives to conventional plastics.

2. Literature Review / Related Work

According to Sood et al. (2015) research on injection-molded sisal fiber composites with a matrix of equal parts virgin and recycled high density polyethylene (HDPE) found that the effect of chemical treatment depended on fiber content. At 30 wt.% fiber, the composite treated with NaOH, benzoyl peroxide, and maleic anhydride reached a tensile strength of 15.75 MPa, about 31% higher than the 11.99 MPa recorded for the NaOH and maleic anhydride treatment. At a much lower loading of 7.5 wt.%, the two treatments performed almost identically, at roughly 19 MPa.

Adding more sisal fiber to polypropylene (PP) made the composites considerably stiffer. At 30 wt.% fiber, tensile Modulus increased by 153%, although tensile strength stayed marginally below that of unfilled PP. Flexural behavior followed a similar pattern: the 30 wt.% composite improved by 9.6% in flexural strength and 55.33% in flexural modulus. Interestingly, impact

strength was higher in composites made without the MAPP coupling agent than in those containing it (Munde et al., 2019).

Sisal fibers were treated with 10% NaOH, neutralized with acetic acid, and bleached with H_2O_2 before being compounded with waste PP. At 15% fiber loading, treated composites reached a peak tensile strength of 19.90 MPa compared to 10.25 MPa for untreated ones (Abebayehu & Engida, 2021).

Sisal fibers were treated with a 2 wt.% sodium bicarbonate solution at 80°C for 2, 4, or 8 hours, and the PP composites were compatibilized with 10 wt.% Polypropylene grafted maleic anhydride (PP-g-MA). The average fiber length of 17.7 ± 5.8 mm was above the critical length of roughly 8 mm. At 40 wt.% fiber, flexural Modulus rose from 734 MPa to 2890 MPa, and flexural strength, tensile strength, tensile modulus, and impact strength rose by 70%, 74%, 52%, and 50% respectively, relative to neat PP. The measured density fell below the theoretical value, which points to voids inside the composite, and elongation at break decreased as fiber content increased, indicating reduced ductility (Bhagat & Ghosh, 2022).

Sisal and banana fibers were chopped to 3 mm, soaked in a 5% NaOH solution, and combined with LY 556 epoxy resin. Composites with a greater proportion of sisal and with treated fibers showed clearly better compressive behavior, which is attributed to the alkali removing impurities from the fiber surface. Compressive strength increased from 322 MPa with untreated fibers to 430 MPa with treated ones (Badyankal et al., 2019).

Composites of pine dust and recycled HDPE were produced by single-screw extrusion at 210°C, using different filler contents and particle sizes. The best tensile strength overall came from medium-sized particles (250-500 μm) at 20 wt.% loading, while elongation fell for every particle size tested. The main drawbacks were porosity, caused by poor adhesion between filler and matrix, and a pronounced drop in ductility (Adhikari et al., 2024).

Experimental findings show that the natural fibre reinforced polymer composite (NFRPC) achieved compression and bending strengths comparable to those of femur bone at fibre contents of 12%, 18%, and 24%, indicating its suitability for orthopaedic implant applications (Virupaksha Gouda et al., 2020).

3. Materials and Methods

Fresh and mature agave leaves were collected from Tarakeshwor, Kathmandu. The spines along their edges were trimmed off. Fibers were then extracted using an underground composting method over 30 days (Giri et al., 2012). Microbial activity broke down the natural binding substances (Eleutério et al., 2025). Once extracted, the fibers were washed thoroughly with water to remove impurities and dried in sunlight for 2-3 days, yielding white, lustrous strands. These were labeled as untreated fibers and set aside for further experimental work.



Figure 1

Agave plant

LDPE-based milk pouches and poly bags were obtained from Om Satya Sai Plastic Industry, located in Bhaktapur Industrial Estate, Bhaktapur. These plastics were first fed into a shredder to reduce them to smaller sizes, after which any remaining water was removed. The shredded plastic was then sun-dried to eliminate residual moisture before being processed through a fine plastic cutter to obtain smaller, uniform pieces.

3.1 Chemical treatment of Agave Fiber

Alkaline treatment improves surface adhesion by eliminating both natural and artificial impurities. More Specifically, NaOH treatment breaks the fibers down into individual fibrils through delignification, removing the cementing compounds, thereby increasing the surface area available for interaction with the polymer matrix (Gudayu et al., 2022; Prome et al., 2025). Fibers were soaked in 6% (w/v) NaOH solution at ambient (room) temperature for about 24 hours. The soaking time allowed activation of the hydroxyl (-OH) groups of lignin and cellulose in the fibers. The chemically treated fibers were then washed repeatedly with distilled water and allowed to dry in sunlight for 24 hours. The sun-dried fibers were further dried in an oven at 60 °C.



Figure 2

Agave fiber obtained after chemical treatment and drying

3.2 Composite preparation

Recycled LDPE (rLDPE) was collected and mixed with short agave fiber of length 5-10 mm at different weight percentages (wt.%), namely 5, 10, 15, and 20 wt.% agave fiber. The samples were mixed using a 0.75 kW grinder-mixer prior to the extrusion process. A total weight of 700 g was used to make each composite sample.



Figure 3

Mixture of Chopped Agave Fibers and recycled LDPE

Table 1

Composition of Recycled LDPE Composites Reinforced with Agave Fiber

Composite Code	Agavefiber(wt.%)	rLDPE (wt.%)	Sample details
rLDPE/AF0	0	100	100% rLDPE and 0% agave fiber
rLDPE/AF5	5	95	95% rLDPE and 5% agave fiber
rLDPE/AF10	10	90	90% rLDPE and 10% agave fiber
rLDPE/AF15	15	85	85% r LDPE and 15% agave fiber
rLDPE/AF20	20	80	80% rLDPE and 20% agave fiber
rLDPE/AF15 untreated	15	85	85% rLDPE and 15% Untreated agave fiber

Note. rLDPE = recycled low-density polyethylene; AF = agave fiber; wt.% = weight percent.

3.3 Fabrication and sample processing

Fabrication of the composite material was done by using Single screw extruder. samples were fed into the extruder through a hopper, Considering the melting temperature of the LDPE to be 115°C the temperature of the heaters was set at 165°C. The specimen was extracted in a die of rectangular cross section of size (500mm ×25mm ×35mm), bolted on the flange of outlet. After that, die was removed from the extruder and was let to cooled in a water to solidify.



Figure 4

Fabricated rLDPE/Agave Fiber Composite Specimen

The fabricated composite materials were carefully machined, cut, and finished using suitable tools to produce test specimens with the required dimensions for mechanical property evaluation.

3.4 Mechanical Testing

3.4.1 Tensile Test

Tensile test was conducted in accordance with ASTM D638 standard specimen. It utilizes standardized, dumbbell shaped (dog-bone) specimens of 165 mm length. DEESHA IMPLEX Universal testing machine (UTM) at crosshead speeds of 50 mm/min at room temperature until failure and then analyzed to calculate the percentage of elongation, ultimate strength, and yield strength of the composite. Three specimens were tested for each composition under each loading condition, and the average values are reported.



Figure 5

Tensile Test Specimens of Agave Fiber-Reinforced rLDPE Composites

3.4.2 Compression test

Rectangular specimen of size 20 mm x 20 mm ×40 mm was prepared. Experiments were executed at room temperature using AMI- UTM. Sample were hold between upper and lower pressure plate. Three specimens were tested for each composition under each loading condition, and the average values are reported Yield and ultimate strength of the specimen is calculated.



Figure 6

Compression Test Specimens of Agave Fiber-Reinforced rLDPE Composites

3.4.3 Morphological analysis

Surface morphology, fiber distribution and adhesion of the fabricated composite was observed by scanning electron microscope (SEM) with 120-200x magnification, using TM3000 Tabletop microscope.

4. Results

4.1 Morphology

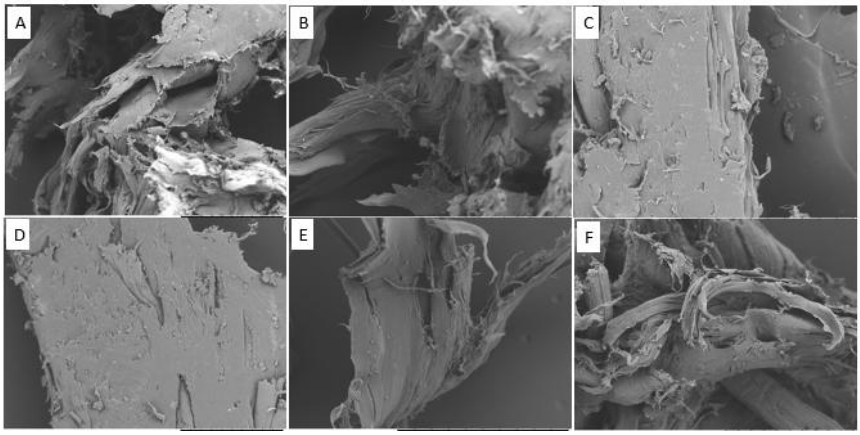


Figure 7

SEM Images of (A) Recycled LDPE matrix, (B) rLDPE and 5wt.% treated agave fiber (C) rLDPE and 10 wt.% treated agave fiber, (D) rLDPE and 15 wt.% treated agave fiber, (E) rLDPE and 20 wt.% treated agave fiber, (F) rLDPE and 15 wt.% untreated agave fiber.

Figure 7- A, neat rLDPE shows smooth, flat, continuous surface with some wrinkling and large rounded masses. In fig. B, the matrix appears as torn, drawn, feathery sheets, with fibers partly aligned along the extrusion direction. In fig. C, a broad, continuous matrix surface with fibers oriented along the extrusion direction can be observed while continuous, compact matrix, with most fibers covered by polymer and fine fibrils visible on the surface of 15 wt.% fiber. A large fiber bundle with a branch, partly detached from the matrix and covered by a thin polymer film in 20% fiber loaded composite. Meanwhile, thick bundles that are twisted, folded and stacked, with a rougher, layered surface, peeled layers, and large gaps between and beneath the bundles is observed in untreated composite sample.

4.2 Tensile test

Table 2, Figure 8 shows neat rLDPE had a proportional limit of 5.5 MPa and Ultimate Tensile Strength of 13.44 MPa, which dropped to ultimate strength 12.29 MPa and proportional limit rise to 8 MPa at 5 wt.% fiber, then rose to ultimate strength of 16.03 MPa where proportional limit remain same at 10 wt.% and peaked at proportional limit of 11 MPa and Ultimate strength to 19.10 MPa at 15 wt.% before falling to Proportional limit strength to 8 MPa and Ultimate strength 13.67 MPa at 20 wt.% Alkali treatment is widely reported to clean and roughen natural fiber surfaces, thereby enhancing mechanical interlocking with the matrix and improving interfacial adhesion (Abebayehu & Engida, 2021) . The untreated 15 wt.% composite reached proportional limit of 7.7 MPa and ultimate strength only 12.40 MPa, and strain at failure generally decreased with fiber content 1.40 at neat rLDPE to 0.74at 20 % fiber loading. Ductility is commonly reported to decline as filler content rises in wood-dust-reinforced composites(Adhikari et al., 2024).

Table 2

Tensile Test Results for Recycled LDPE Composites with Varying Agave Fiber Content

Composite	Proportional limit stress (MPa)	Ultimate tensile strength (MPa)	Strain at failure (%)
rLDPE/AF0	5.5	13.44	1.40
rLDPE/AF5	8	12.29	1.12
rLDPE/AF10	8	16.03	1.18
rLDPE/AF15	11	19.10	0.97
rLDPE/AF20	8	13.67	0.74
rLDPE/AF15 Untreated	7.5	12.40	0.60

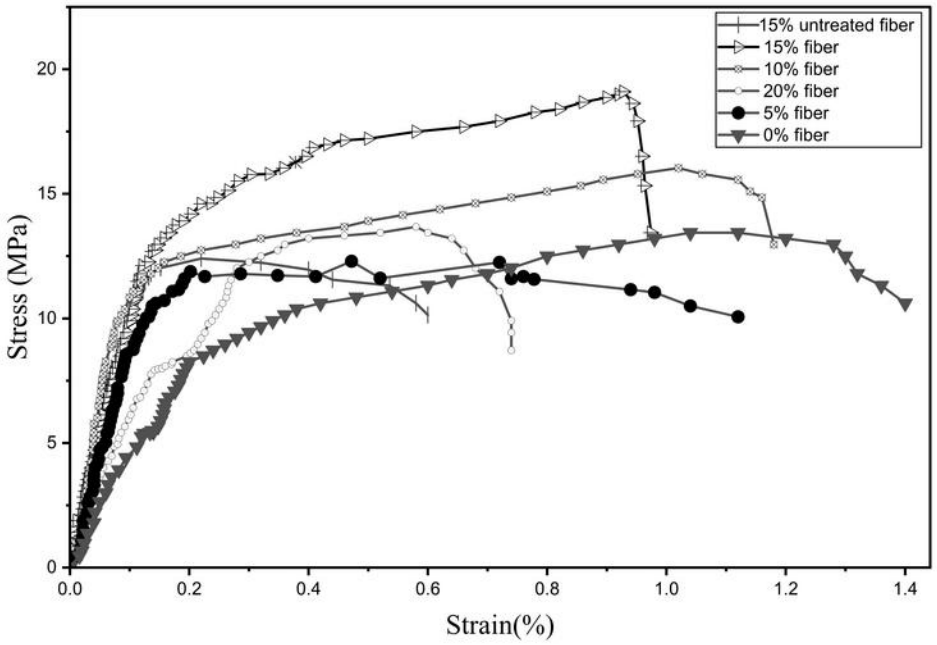


Figure 8

Stress-Strain Behavior of Recycled LDPE Composites at Different Agave Fiber Contents

4.3 Compression test

Table 3, Figure 9 show Neat rLDPE had a compressive strength of 15 MPa and a yield strength of 7 MPa. Compressive strength fell to 12 MPa at 5 wt.%, recovered to 15.5 MPa at 10 wt.%, and peaked at 19 MPa at 15 wt.%, with yield strength rising to 10 MPa. At 20 wt.% compressive strength fell to 12.5 MPa, and the untreated 15 wt.% composite reached only 11 MPa, so the treated composite was about 73% higher.

Table 3

Yield and Compressive Strength of Recycled LDPE Composites with Varying Agave Fiber Content

Specimen	Yield strength (MPa)	Compressive strength (MPa)
rLDPE/AF0	7	15
rLDPE/AF5	9	12

rLDPE/AF10	8	15.5
rLDPE/AF15	10	19
rLDPE/AF15 Untreated	7	11
rLDPE/AF20	8	12.5

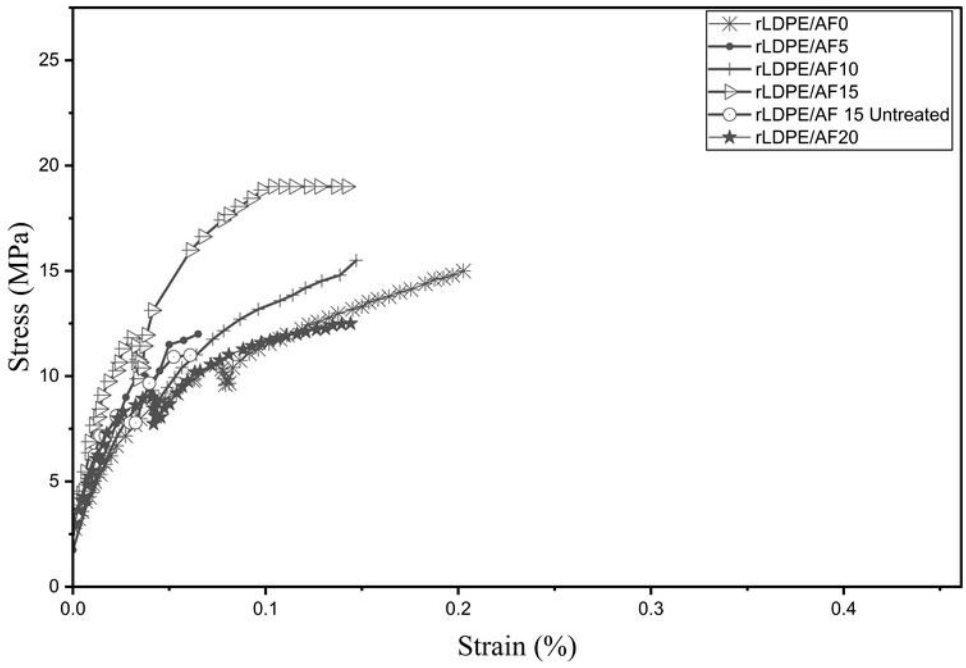


Figure 9

Compressive Stress-Strain Behavior of Recycled LDPE Composites at Different Agave Fiber Contents

5. Discussion

5.1 Morphology

The drawn, feathery sheets show the matrix deformed in a ductile way. This fits the high strain at failure of neat and low fiber samples. A compact matrix with fibers encapsulated suggests good wetting and fiber and matrix contact due to result of surface modification, a detached bundle with only a thin film around it points to weak adhesion. Cavities. gaps and peeled layers suggest incomplete wetting, Poor interfacial adhesion may account for the noticeable surface irregularities and the cavities and voids observed in the material (Aiyejagbara et al., 2024). The untreated fibers reduced ultimate strength of the composite was linked to pronounced particle agglomeration when the pine dust content was high (Adhikari et al., 2024) . More fibers, and weaker bonding, lead to less ductility (Putri Parahdiba et al., 2026) .

5.2 Tensile test

Strength increased up to 15 wt.% because of effective stress transfer from the matrix to well bonded fibers, while at 20 wt.% agglomeration and voids reduced it. Alkali treatment improved fiber-matrix adhesion, explaining the 54% higher UTS than the untreated composite, while the rigid fibers reduced ductility (Aravinth et al., 2023) .

5.3 Compression test

The peak at 15 wt.% indicates efficient load transfer through well-bonded fibers, while the lower values at 20 wt.% are consistent with agglomeration and voids. The much lower strength of the untreated composite suggests weak fiber-matrix adhesion, showing that alkali treatment improves the interface (Badyankal et al., 2019) **.** Reinforcing waste LDPE with carbonized natural fillers such as bamboo has been proposed as a route to higher compressive strength and wider applications, including flooring and furniture surfaces (Ndukwe et al., 2022) .

6. Limitations

The treated and untreated samples were compared at 15 wt.% only, and only one NaOH concentration (6%) and one soaking time were used. The specimens were produced by single-screw extrusion into a die, and the results are specific to this process. Other techniques, such as twin-screw extrusion, compression molding, or injection molding, and the incorporation of a compatibilizer such as maleic anhydride, may give different fiber dispersion, orientation, and void content, and therefore different mechanical properties.

7. Conclusion

This study showed that NaOH-treated agave fiber at 15 wt.% gave the best tensile and compressive strength in recycled LDPE composites. Alkali treatment removes lignin, hemicellulose, and wax from the fiber surface, which improves the adhesion between the hydrophilic fiber and the hydrophobic polymer matrix and allows more effective stress transfer. The resulting material is lightweight, low-cost, and eco-friendly, making it a promising candidate for non-structural or semi-structural applications while also supporting sustainable waste management through the reuse of recycled LDPE and natural fiber.

8. Acknowledgments

The authors wish to acknowledge the Department of Mechanical and Automobile Engineering (Thapathali Campus), the Research Centre for Applied Science and Technology (RECAST), Tribhuvan University, National Innovation Centre Nepal, (NIC), kirtipur, and Hisi Polypipe (Balaju Industrial District), Tianjin University, China for their generous provision of laboratory space and technical facilities essential to this research.

9. Funding

The author(s) received no financial support for the research, authorship, or publication of this paper.

10. Conflict of Interest

The author(s) declare no conflict of interest.

11. Author Contributions

R. M. Lamichhane: Conceptualization, Methodology, Investigation, Formal analysis Writing original draft.

S. P. Adhikari: Supervision, Validation, Writing, review, editing, Project administration.

12. Data Availability

The data supporting the findings of this study are available on reasonable request.

13. References

Abebayehu, S. G., & Engida, A. M. (2021). Preparation of Biocomposite Material with Superhydrophobic Surface by Reinforcing Waste Polypropylene with Sisal (Agave sisalana) Fibers. *International Journal of Polymer Science*, *2021*. https://doi.org/10.1155/2021/6642112

Adhikari, S. P., Pandey, U., & Adhikari, R. (2024). Effect of filler particle size on of pine dust-filled recycled HDPE composites. *UNEC Journal of Engineering and Applied Sciences*, *4*(2), 91–99. https://doi.org/10.61640/ujeas.2024.1209

Aiyejagbara, M. O., Onyemachi, D. I., Ibeneme, U., Uteno, J. E., & Simon, C. E. (2024). *STUDY ON THE TRIBOLOGICAL , HARDNESS , AND MORPHOLOGICAL PROPERTIES OF RECYCLED LOW-DENSITY*. *2*(1), 205–213.

Ali, S. S., Xiong, M., Jiao, H., Al-Tohamy, R., & Sun, J. (2026). Recent advances in plastic waste management: A systems-level framework for circular plastic economy strategies—A state-of-the-art review. In *Journal of Environmental Management* (Vol. 404). Academic Press. https://doi.org/10.1016/j.jenvman.2026.129282

Aravinth, K., Kondusamy, V., Ramakrishnan, T., Tamilarasan, V. D., & Kavi Rasu, K. (2023). Investigation of mechanical properties on agave plant fiber composite by experimental and numerical methods. *Materials Today: Proceedings*. https://doi.org/10.1016/j.matpr.2023.07.054

Badyankal, P. V., Manjunatha, T. S., Vaggar, G. B., & Praveen, K. C. (2019). Compression and water absorption behaviour of banana and sisal hybrid fiber polymer composites. *Materials Today: Proceedings*, *35*, 383–386. https://doi.org/10.1016/j.matpr.2020.02.695

Bhagat, A. B., & Ghosh, A. K. (2022). Performance Properties of PP/Sisal Fibre Composites having Near Critical Fibre Length and Prediction of Their Properties. *Fibers and Polymers*, *23*(7), 1983–1994. https://doi.org/10.1007/s12221-022-4086-3

Dokl, M., Copot, A., Krajnc, D., Fan, Y. Van, Vujanović, A., Aviso, K. B., Tan, R. R., Kravanja, Z., & Čuček, L. (2024). Global projections of plastic use, end-of-life fate and potential changes in consumption, reduction, recycling and replacement with bioplastics to 2050. *Sustainable Production and Consumption*, *51*, 498–518. https://doi.org/10.1016/j.spc.2024.09.025

Eleutério, T., Trota, M. J., Meirelles, M. G., & Vasconcelos, H. C. (2025). A Review of Natural Fibers: Classification, Composition, Extraction, Treatments, and Applications. In *Fibers* (Vol. 13, Number 9). Multidisciplinary Digital Publishing Institute (MDPI). https://doi.org/10.3390/fib13090119

Giri, J., Le, H. H., Radusch, H.-J., Lach, R., Grellmann, W., Lebek, W., & Adhikari, R. (n.d.). *Effect of Ketuki Fiber on Morphology and Mechanical Properties of Thermoplastics Composites*.

Gudayu, A. D., Steuernagel, L., Meiners, D., & Gideon, R. (2022). Effect of surface treatment on moisture absorption, thermal, and mechanical properties of sisal fiber. *Journal of Industrial Textiles*, *51*(2), 2853S-2873S. https://doi.org/10.1177/1528083720924774

Huang, S., Dong, Q., Che, S., Li, R., & Tang, K. H. D. (2025). Bioplastics and biodegradable plastics: A review of recent advances, feasibility and cleaner production. In *Science of the Total Environment* (Vol. 969). Elsevier B.V. https://doi.org/10.1016/j.scitotenv.2025.178911

Macheca, A. D., Mutuma, B., Adalima, J. L., Midheme, E., Lúcas, L. H. M., Ochanda, V. K., & Mhlanga, S. D. (2024). Perspectives on Plastic Waste Management: Challenges and Possible Solutions to Ensure Its Sustainable Use. In *Recycling* (Vol. 9, Number 5). Multidisciplinary Digital Publishing Institute (MDPI). https://doi.org/10.3390/recycling9050077

Mendoza, J. E., Tineo, D., Chuquibala-Checan, B., Atalaya-Marin, N., Taboada-Mitma, V. H., Tafur-Culqui, J., Tarrillo, E., Gómez-Fernández, D., Goñas, M., & Reyes-Reyes, M. A. (2024). Global perspectives on the biodegradation of LDPE in agricultural systems. In *Frontiers in Microbiology* (Vol. 15). Frontiers Media SA. https://doi.org/10.3389/fmicb.2024.1510817

Munde, Y. S., Ingle, R. B., & Siva, I. (2019). Effect of sisal fiber loading on mechanical, morphological and thermal properties of extruded polypropylene composites. *Materials Research Express*, *6*(8). https://doi.org/10.1088/2053-1591/ab1dd1

Ndukwe, A. I., Umoh, S., Ugwochi, C., Ogbuji, C., Ngolube, C., Aliegu, F., & Izuegbu, L. (2022). PREDICTION OF COMPRESSION STRENGTH OF BAMBOO REINFORCED LOW-DENSITY POLYETHYLENE WASTE (LDPEw) COMPOSITES. *Composites Theory and Practice*, *2022*(3), 142–149. https://doi.org/10.62753/ctp.2022.04.3.3

Prome, F. S., Hossain, M. F., Rana, M. S., Islam, M. M., & Ferdous, M. S. (2025). Different chemical treatments of natural fiber composites and their impact on water absorption behavior and mechanical strength. *Hybrid Advances*, *8*. https://doi.org/10.1016/j.hybadv.2025.100379

Putri Parahdiba, N., Anam, K., Gapsari, F., & He, R.-E. (2026). *EFFECT OF ALKALI TREATMENT ON MECHANICAL AND THERMAL PROPERTIES OF SISAL FIBER FOR COMPOSITE APPLICATIONS*. 59–68. https://doi.org/10.21776/MECHTA.2026.007.01.7

Ramachandran, A. R., Mavinkere Rangappa, S., Kushvaha, V., Khan, A., Seingchin, S., & Dhakal, H. N. (2022). Modification of Fibers and Matrices in Natural Fiber Reinforced Polymer Composites: A Comprehensive Review. In *Macromolecular Rapid Communications* (Vol. 43, Number 17). John Wiley and Sons Inc. https://doi.org/10.1002/marc.202100862

Shekar, S., & Ramachandra, M. (2018). Green Composites: A Review. In *Materials Today: Proceedings* (Vol. 5). www.sciencedirect.comwww.materialstoday.com/proceedings2214-7853

Singh, N., & Walker, T. R. (2024). Plastic recycling: A panacea or environmental pollution problem. *Npj Materials Sustainability*, *2*(1). https://doi.org/10.1038/s44296-024-00024-w

Sood, M., Dharmpal, D., & Gupta, V. K. (2015). Effect of Fiber Chemical Treatment on Mechanical Properties of Sisal Fiber/Recycled HDPE Composite. *Materials Today: Proceedings*, *2*(4–5), 3149–3155. https://doi.org/10.1016/j.matpr.2015.07.103

Utekar, S., V K, S., More, N., & Rao, A. (2021). Comprehensive study of recycling of thermosetting polymer composites – Driving force, challenges and methods. In *Composites Part B: Engineering* (Vol. 207). Elsevier Ltd. https://doi.org/10.1016/j.compositesb.2020.108596

Virupaksha Gouda, H., Channabasavaraj, S., Gouda, A. T., & Mahendra, K. C. (2020). Experimental investigation on compression and bending properties of epoxy composites reinforced with Al2O3, kenaf/hemp fibers for orthopaedic implants. *IOP Conference Series: Materials Science and Engineering*, *988*(1). https://doi.org/10.1088/1757-899X/988/1/012001

SOLVOTHERMAL SYNTHESIS AND ELECTROCHEMICAL PERFORMANCE OF A TRIMETALLIC Co-Ni-–Zn MOF@MnO_2 COMPOSITE FOR SUPERCAPACITOR APPLICATIONS

Kushal Chuwain [1,] Sachin Ghimire [1] Chhabi Lal Gnawali1* [1]

[1]Department of Applied Sciences and Chemical Engineering, Pulchowk Campus, Institute of Engineering, Tribhuvan University, Nepal

1. Department of Applied Sciences and Chemical Engineering, Pulchowk Campus, I.O.E., T.U.

*Correspondence author; email: chhabig123@ioe.edu.np; +977-9851123099

Abstract

Trimetallic metal–organic frameworks (MOFs) have gained interest as electrode materials because combining different metal centers can improve their structural and electrochemical properties. In this study, a Ni–Co–Zn MOF was prepared hydrothermally from nickel, cobalt, and zinc nitrates using 2-methylimidazole in methanol. The reaction mixture was stirred at room temperature, heated at 120 °C for 24 h, washed, and vacuum-dried at 80 °C. XRD results confirmed the successful formation of a crystalline mixed-metal framework. Electrochemical measurements revealed mainly pseudocapacitive behavior for the Ni–Co–Zn MOF, whereas MnO_2 showed predominantly EDLC behavior. Incorporating MnO_2 with the MOF enhanced the overall electrochemical performance. The optimized Ni–Co–Zn MOF/MnO_2 composite delivered a specific capacitance of 712 F g^{-1}, 24.72 W h kg^{-1}, power density of 248.27 W kg^{-1}at 1 A g^{-1}, highlighting its potential for high-performance supercapacitor applications.

Keywords: Ni–Co–Zn MOF; Trimetallic MOF; Solvothermal synthesis; Supercapacitors;

Introduction

The requirement of energy continues to increase because of huge population growth; it becomes urgent need for environmentally friendly technologies for a cleaner and more durable energy future [1]. the climate change is also the developing issue and many countries are changing to wind and solar energy to reduce the fossil fuel consumption, however because of source depend on different weather condition, so efficient energy system is required for energy storage [1]. The main aim of energy storage system is collecting the energy from different source, modify it and changing into various application [2]. therefore, nowadays there has been growing interest on high energy density and high-power density system, which is better solution to defeat the problems regarding on energy storage system [3]. supercapacitors are helpful with regard to longer stability high power density, low cost, fast charge-discharge etc [4]. batteries have normally high energy density and low power density but supercapacitors have high power density and relatively lower energy density than batteries [5]. Supercapacitors have ability to store and provide faster energy transfer and they are made of from electrodes ,separator and electrolytes, separator separates electrodes electrically and their electrical materials depend on electrical properties[6], [7].on the basis of energy storage and ion distribution of electrolyte from surface area of the electrodes there are three types of capacitors electric double layer capacitors(EDLC),pseudo capacitor and hybrid capacitor[8].the charge storage mechanism of EDLC is electrostatic or non-faradic mechanism[9].pseudo capacitors store charge via faradic mechanism that involves the charge transfer between electrode and electrolyte[10].Hybrid supercapacitors are combination of EDLC and pseudo capacitors which have more enhanced

properties for charge storage[11] .in comparison with pseudo capacitors and EDLC, hybrid capacitors have higher power density as well as energy density[12].Ragon curve visually gives idea about how energy density and power density relate for different types of energy storage system to compare performance profiles[13].Metal organic framework MOFs are formed by coordination of metal ions and organic linker and forms highly ordered, tunable structure [14]. MOFs are most suitable precursors of hybrid supercapacitors electrode material due to their enhanced electrochemical performance [15].the mostly commonly used metals are transition metals and organic linkers are 2 methyl imidazole ,benzene dicarboxylic acid etc.[16].in this framework metal acts as node and organic linker provide frameworks geometry[17].they have extraordinary properties like chemical versatility ,tunable pore size and make them reliable candidates for energy storage ,gas storage ,catalysis, sensing etc[18], [19], [20], [21], [22].To enhance the energy storage there are different multi metals are used in practice i.e. are monometallic, bimetallic ,trimetallic and multi metallic MOFS[23], [24].the synthesis route of metal organic framework is main factor for their functional as well as structural properties of MOFS for applications like as energy storage[25].the main methods are Solvothermal synthesis, Hydrothermal synthesis, Microwave-Assisted Synthesis, mechanochemical synthesis, Sonochemical synthesis[26], [27], [28], [29], [30]. The solvothermal synthesis involves dissolving the metal salts in an organic solvent and heating at elevated pressure at 80-150 °C in a closed vessel. Slow crystallization under control conditions facilitates the growth of highly crystalline MOFs, which have large crystals and high internal surface area [31], [32]. when water is used as a solvent during the synthesis of MOFS then this method is known as hydrothermal method. Hydrothermal and solvothermal methods are most common synthesis method of metal organic framework methods. Solvothermal method is best method of synthesis rather than hydrothermal due to controlled morphology structure is formed and as well as large surface area product is formed[33], [34].although Metal–Organic Frameworks (MOFs) have large surface area, tunable structure, high porosity but in practical in energy storage ,environmental remediation is limited due to low chemical stability ,poor electrical conductivity etc, to minimize from these drawback the incorporation of MOFS with functional composite materials is best way[35], [36]. Metal oxides like $NiCoO_4$, MnO_2, Co_3O_4, and NiO are pseudo capacitance in nature with high theoretical value of specific capacitance and redox activity .when they are combine with metal oxides due to synergistic effect metal oxides have additional redox sites and pseudo capacitance and compensate MOFs poor conductivity[37], [38].Manganese dioxide is a very good candidate for supercapacitors because it is low cost materials, environment friendly or easily available and outstanding electrochemical performance[39], [40].since Mno_2 is an EDLC and less pseudo capacitive materials and its charge storage process is fast and reversible via redox recations.it is highly polymorphic in nature and due to improved capacity ,it shows greater ion diffusion and electrochemical activity[41].the fabrication of these type of composites typically includes methods like as hydrothermal synthesis, solvothermal synthesis that allow precise control over morphology ,their particle size and composition to optimize ion and electron transport[42]. The incorporation of Ni and Co centers is relevant to the alkaline electrochemical reactions, while the incorporation of Zn can affect the framework formation and local structure. Zinc is mainly used for designed variable. In addition to the redox chemistry of MnO_2, the electrochemical utilization of this material is dependent on the thickness, morphology and electrolyte accessibility [43], [44], [45]. Previously, Ni–Co–Zn trimetallic MOFs have been shown to be electrodes for supercapacitors, such as architectures prepared using carboxylate linkers [46]. In this work, a different synthetic approach is presented, by combination of Ni–Co–

Zn material, linked to 2-methylimidazole, with MnO_2, synthesized using a solvothermal method. The goal is to see how the electrochemical response of the MOF performs with a series of fixed loadings of MnO_2 and determine the loading conditions that yield the highest reported specific capacitance for this prepared composite.

2.materials and experimental methods.

Nickel (II) nitrate hexahydrate (98.0%), Zinc nitrate hexahydrate (98.0%), Cobalt nitrate hexahydrate (98.0%) was used for MOF precursors. All three reagents were purchased from HI media Laboratories Pvt. Ltd. 2 -Methyl Imidazole was purchased from Sigma Aldrich Germany Co. for organic linker. Methanol and Ethanol were purchased from Changshu Hongsheng Fine Chemical Co., Ltd. Poly (vinylidene fluoride) (PVDF) was purchased from Sigma Aldrich Germany Co, activated carbon and N-methyl-2-pyrrolidone (NMP) was purchased from Prayog Fine Chemical Hyderabad India. were used in electrode preparation. 99.0%$KMnO_4$(LOBA Chemie Pvt.Ltd). 1.93401.0521EMPLURAabout 35%HCl Merck Ni foam, activated carbon, Reagent-grade DI water all were purchased from Biotech trading concern Nepal Tripureswor Ktm. All the chemicals and solvents used during this research were of analytical grade. the entire synthesis of the composite was conducted at Functional Nanomaterial Processing Lab at Central Department of Chemistry. All The procedure was adapted from common bimetallic metal organic framework synthesis and extended to trimetallic.

2.1. Preparation of organic linker solution

328.4 milli gram (4 mmol) 2-methyl imidazole was weighed first, after that this solid is transferred into beaker. Dissolved this solid in 20 mL of methanol. Stirred this continuously until the solution becomes clear.

2.2. Preparation of metal solution

Zn $(NO_3)_2 \cdot 6H_2O$: (0.85 mmol) mol.wt (297.49 g,Co $(NO_3)_2 \cdot 6H_2O$: (0.10 mmol) (291.03 g) and Ni $(NO_3)_2 \cdot 6H_2O$: (0.05 mmol) mol.wt (290.79 g) were weighed in different beaker. Dissolved the total weighed metal salts in 50 mL of methanol. Stirred for 10-15 minutes until fully dissolved. The solution was pale green color. In a 100 mL beaker, a moderate-magnetic-stirring pour of ligand Solution was made. After that Slowly added metal solution dropwise into the beaker containing ligand Solution. there was the formation of a precipitate or a cloudy solution almost immediately. Then the mixing was continued for 24 hours at room temperature to ensure complete mixing. Gently pour all the milky material into a 100 mL Teflon-lined autoclave. Sealed the autoclave.

2.3. Solvothermal Treatment

Put the sealed autoclave into pre-heated laboratory oven. Heated at 120 °C for 24 hours. Turn off the oven after 24 hours and allow to cool to room temperature for 6-8 hours. Sunk to the bottom was the solid product. It was vacuum dried after 24 hours at 80 °C after four times filtering and washing by deionized water. The powder formed from the nickel zinc cobalt was light green in color.

2.4 Synthesis of MnO_2:

At first, 4.115 g of $KMnO_4$ was added to about 70 mL of deionized water, and then thoroughly stirred at room temperature for 10 minutes. Further, 3.405 mL of concentrated HCl was added to this solution with constant stirring. After cooling, the autoclave was left to cool down to room

temperature. The product as obtained was separated through centrifugation. Then the impurities were washed off through deionized water several times before it was cleaned using ethanol and it was then dried in air at a temperature of 90 ˚C for 1 hour. The final product was a brown black MnO_2 powder.

2.5 Synthesis of Ni–Co–Zn MOF/MnO_2 composite

Initially, Ni–Co–Zn MOF (2 mmol) was dispersed in 50 mL of methanol and magnetically stirred for 30 minutes. Separately, MnO_2 (2 mmol) was dispersed in 50 mL of methanol. The two dispersions were combined and sonicated for 15 minutes Solvothermal treatments were performed at 120 °C for 12 h in the mixtures which were then cooled down, washed with methanol and anhydrous ethanol three times and dried at 60 °C. Ni–Co–Zn MOF/MnO_2 was obtained, respectively. The same procedure was repeated using 4 and 6 mmol of MnO_2, while the amount of Ni–Co–Zn MOF and all other preparation conditions were kept constant. The products were designated Ni–Co–Zn MOF/MnO_2 (1), (2) and (3), respectively.

2.6 Preparation of working electrode

Nickel foam (1 cm^2) was taken after that ultrasonically cleaned in 1 M HCl and in deionized water for 10 min. at at 60 °C cleaned foam was dried for 1 h and weighed. After carefully weighing 4 mg (80 wt %) of the active material, 0.4 mg (10 wt %) of binder (PVDF), and 0.4 mg (10 wt %) of conductive additive (Active Carbon), a fine slurry was created by adding NMP solvent dropwise with a mortar and pestle for at least five minutes. The slurry was uniformly coated onto the cleaned nickel foam, dried between coatings, and pressed overnight using aluminum foil. The prepared electrode was weighed and immersed in 3 M KOH for at least 3 hours before electrochemical testing. Separately, the same process was used to prepare the working electrode for pure Ni MOF and other composites.

3.Structural and electrochemical characterization

Powder XRD was used to examine crystalline features. The XRD patterns of all the samples were obtained from a Rigaku Ultima Plus X-ray diffractometer (Rigaku Co. ltd Japan) operated at 40 kV and 90 mA with CuKα radiation (λ = 0.154 nm).CV and GCD were used to compare the electrochemical behavior of the prepared MOF, MnO_2 and the composite electrodes in alkaline electrolyte. The electrochemical performance of the electrode materials was analyzed using a three-electrode cell with a prepared active material as the working electrode, Hg/HgO as the reference electrode, and Pt wire as the counter electrode. each electrode was examined using a 3 M KOH solution. Electrochemical characterization assesses the electrochemical behavior of materials under different conditions. The potential range was within 0 to 0.5 volts. and current density range was from $1Ag^{-1}$to$10Ag^{-1}$.

The following formula is used to determine the specific capacitance of electrodes based on charge-discharge curves [47].

$$C = \frac{I \times \Delta t}{m \times \Delta V} \quad \ldots\ldots\ldots\ldots\ldots\ldots\ldots\ldots\ldots\ldots\ldots\ldots\ldots\ldots \text{(i)}$$

Where m is an active mass, ΔV is a potential window, I is discharge current and Δt is discharging time.

Energy density (W h kg^{-1}): It is the amount energy; the device can store per unit mass or volume [48]. It is mathematically denoted by:

E = …… (ii)

Where, Cs = specific capacitance and

ΔV = potential window

Power density (W kg^{-1}): The amount of power the device can deliver per unit mass per volume. Mathematically it is denoted by:[49], [50]

P = …… (iii)

Where, E= energy density and

Δt = discharge time

4.Results and Discussion

4.1 XRD (x-ray diffraction method)

The composition and crystalline structure of Ni–Co–Zn MOF, MnO_2, Ni–Co–Zn MOF/MnO_2 analysed using the X-ray Diffraction technique in the range of 5-80 degrees, as shown in fig.1

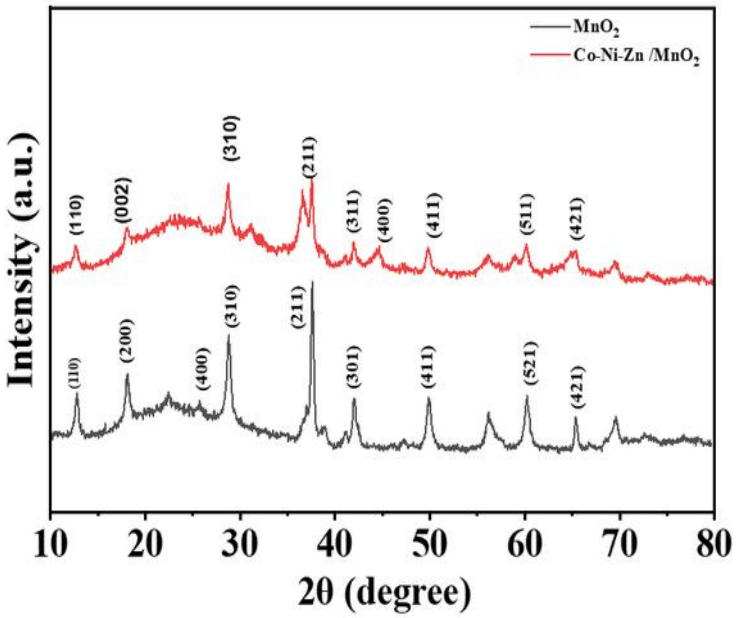
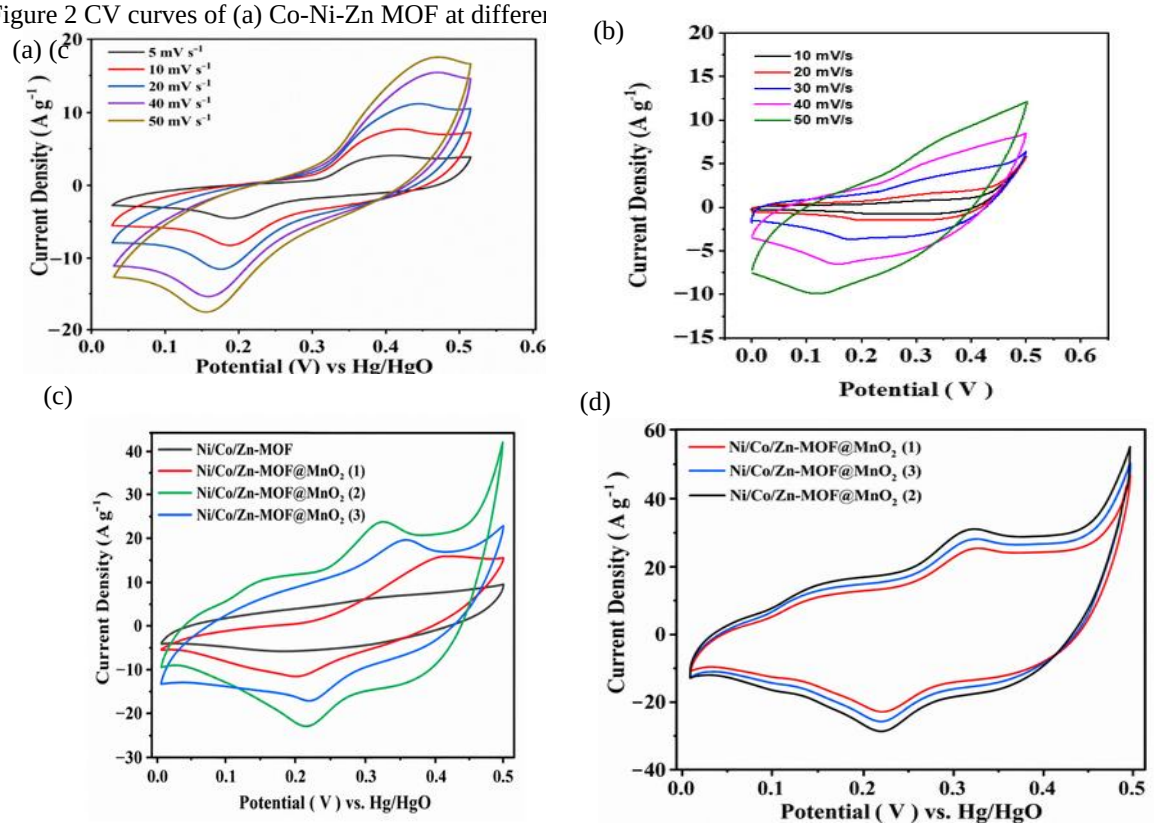


Figure 1 XRD patterns of, MnO_2 Ni–Co–Zn MOF/MnO_2

The diffraction pattern of pristine MnO_2 exhibits prominent reflections at approximately 12.7°, 18.1°, 28.8°, 37.5°, 41.9°, 49.8°, and 60.2°, which can be indexed to the (110), (200), (310), (211), (301), (411), and (521) crystallographic planes, respectively, of tetragonal α-MnO_2 (JCPDS No. 44-0141). These characteristic reflections indicate that the compound is crystallized as MnO_2. After the incorporation of MnO_2 into the composite based on Co–Ni–Zn MOF, several characteristic diffraction peaks are still observed, suggesting that the crystal structure of MnO_2 is maintained. But significant intensity variation and peak broadening is seen in the composite as compared to the pristine MnO_2. These differences are likely due to shifts in crystallite size, structural disorder, or MnO_2/MOF interactions. The wide diffraction lines in the composite, especially in the low angle region could also be due to poorly crystallized material [51], [52].

4.2 Cyclic voltammetry

Figure 2 CV curves of (a) Co-Ni-Zn MOF at differe



The cv profile of CV curves of (a) Co-Ni-Zn MOF at different scan rate, (b) MnO2, at different scan rate (c) comparison of CV of Co-Ni-Zn MOF, Co-Ni-Zn MOF1-3 and (d) Co-Ni-Zn MOF_{1-3} were shown in figure 2.CV curves give the idea about charge storage behaviour, electrochemical nature and influence of Mno_2 incorporation on the electrochemical performance on the synthesized material [53]. In Fig. (a), the CV profiles of the Co–Ni–Zn MOF electrode were recorded at different scan rates ranging from 5 to 50 mV s^{-1}. The curves show distinguishable anodic and cathodic features, which indicates the contribution of Faradaic redox reactions to the charge-storage mechanism pseudo capacitance in nature [54]. Figure 1(b) displays the CV curves of the MnO_2 electrode at scan rates of 10–50 mV s^{-1}which shows rectangular profiles slightly EDLC behavior .CV response of Co–Ni–Zn MOF, Co–Ni–Zn MOF/MnO_2 (1-3) is compared in figure (c). When the MOF electrode is modified with MnO_2, the electrochemical response of the electrode is significantly changed. As an example, sample Co–Ni–Zn MOF/MnO_2 (2) shows the highest enclosed CV area and current response among the investigated composites, indicating the higher charge-storage capacity under the same conditions of measurement. Figure 1(d) further compares the CV profiles of the Co–Ni–Zn MOF@MnO_2

(1), (2), and (3) electrodes. Of these, the sample (2) has the highest positive current response near the upper potential limit while the sample (1) has a relatively smaller response. Based on these observations, influence of the optimization of the content of MnO_2 on electrochemical activity of the composite electrodes was observed. Agglomeration of particles, poor ion transport or high electrical resistance may occur due to excessive MnO_2 loading [55], [56].

4.3. Galvanostatic charge discharge

The charge–discharge (GCD) curves of the Co-Ni-Zn-MOF at different current densities, (b) Mno_2 at different current densities at various current densities (1, 2, 3, 5, and 10 A g^{-1}) between 0 and 0.5 V (vs. Hg/HgO) are shown in Figure 3. The GCD curves exhibit nonlinear charge–discharge characteristics with voltage plateaus, indicates the pseudo capacitance behaviour.ng the involvement of Faradaic redox reactions in the electrochemical energy-storage process. This behavior is indicative that the electrode largely possesses a pseudo capacitance behavior instead of perfect electric double-layer capacitance. The discharge time is the longest at a current density of 1 A g−1, which is a relatively high charge-storage capacity when the current is small. At 1 A g−1 the discharge time is highest for sample 2 and the charge and discharge time decreases from 1 to 10 A g^{-1} which is shown in given fig d. this can be explained by the electrolyte-ion diffusion time being shorter, as well as a decrease in the electroactive sites. The overall results of GCD reveal the electrochemical activity and current dependent charging storage properties of the electrode material, which indicates the great potential of the electrode material for energy storage applications [57], [58], [59], [60].

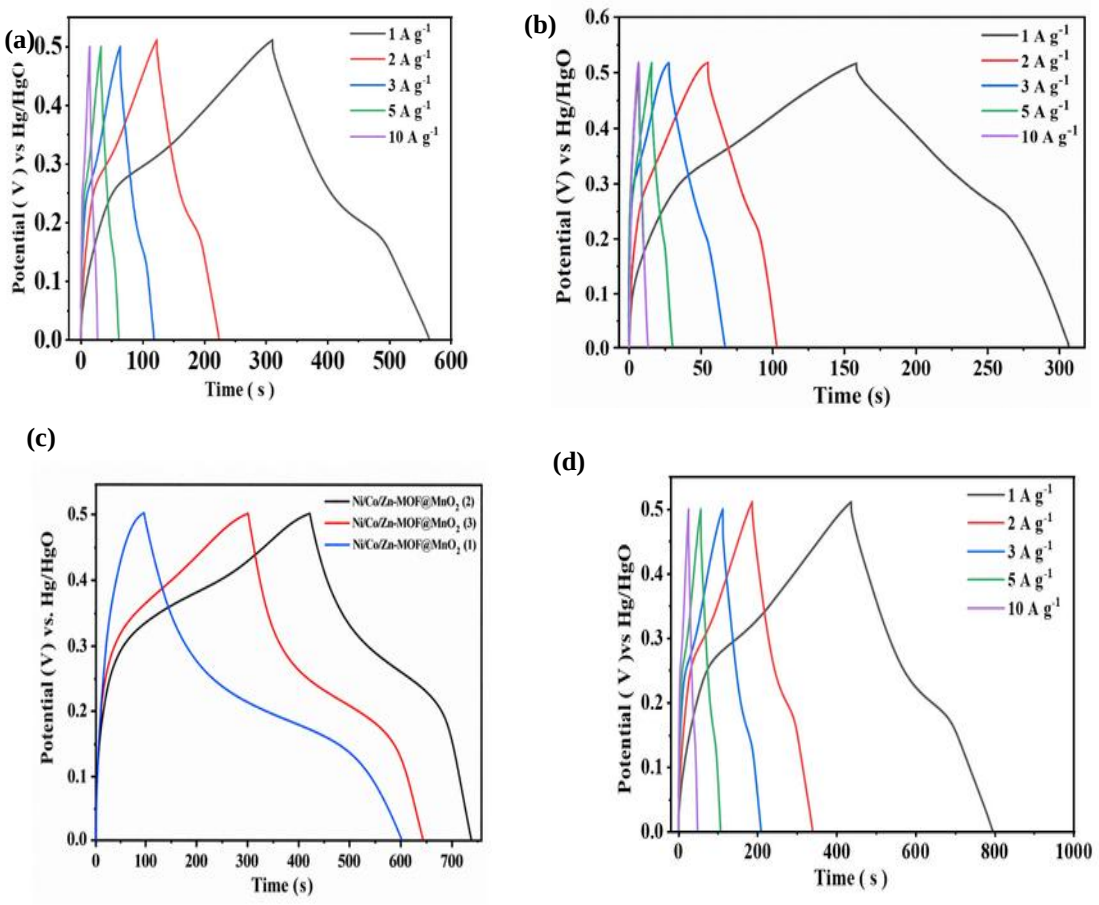


Figure 3: (a) Co-Ni-Zn-MOF at different current densities, (b) Mno_2 at different current densities, (c) Co-Ni-Zn-MOF /Mno_2, (1-3), at 1 $Ag^{-1}$and (d) Co-Ni-Zn-MOF/ Mno_2, (2) at different current densities

From the above GCD graph by using Figure 3.d. the link between an electrode material's specific capacitance (F g^{-1}) and current density (A g^{-1}), obtained using GCD tests is shown in figure 4. largest specific capacitance at 1 A g^{-1}. This is due to electrolyte ions have more time to permeate into the pores and reach the electrode material's active sites also at lower current densities. Therefore, the highest charge storage capacity is obtained [61].

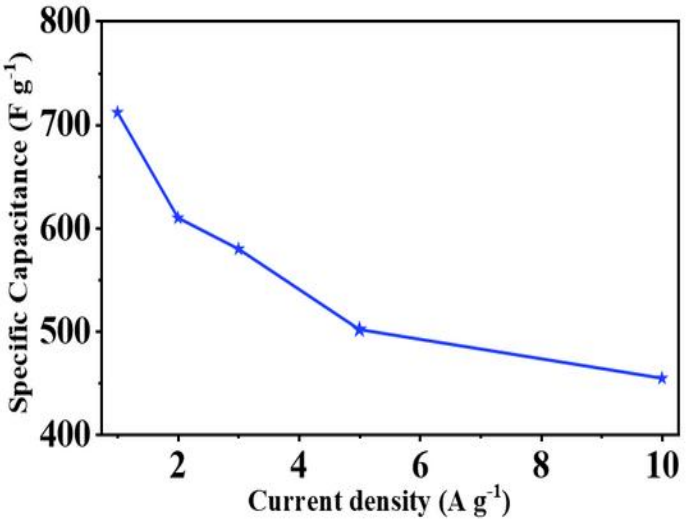


Figure 4 specific capacitance vs current densities

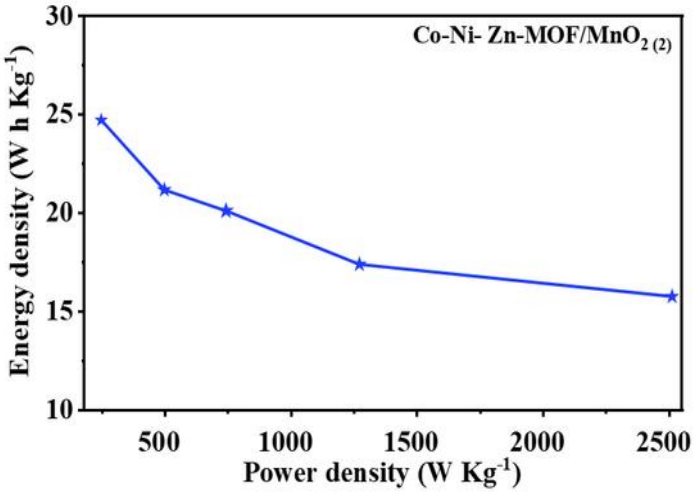


Figure 5 Ragon plot

The Figure 5. shows a Ragone plot of Co-Ni-Zn MOF/MnO_2(2) at 1 A g^{-1} a high energy density of 24.72 W h kg^{-1} at a power density of 248.27 W kg^{-1}. When at current density 10 A g^{-1}, the electrode material has a high-power density of 2512 kW kg^{-1} and energy density of 15.78W h kg^{-1}.

Table 1: Specific Capacitance, Energy Density, and Power Density of electrode materials

Electrode Material	Specific Capacitance (C_{sp}) (Fg^{-1})	Energy Density ($WhKg^{-1}$)	Power Density (Wkg^{-1})
Co-Ni-Zn MOF	506	17.55	249.27
Co-Ni-Zn MOF/MnO_2(2)	712	24.72	248.58

4. Conclusions

The storage of energy has become a global matter with respect the increasing demand for energy. The main purpose of this project is to support this global approach. A series of Ni–Co–Zn MOF/MnO_2 was synthesized from solvothermal process. The XRD methodology suggests the presence of chemically and crystallographically various constituents, while the CV and GCD measurements suggest a compositional dependence of the Faradaic charge-storage response that is pseudo capacitance behavior. whereas MnO_2 showed predominantly EDLC behavior The highest sample performance was measured to be 712 F g-1, at 1 A g-1 high energy density of 24.72 W h kg^{-1} at a power density of 248.27 W kg^{-1}.

5. Conflict of Interest

No conflict of interest.

6.Acknowledgement

I kushal chuwain would like to acknowledge Nanomaterials Lab & Department of Applied Sciences and Chemical Engineering, Pulchowk Campus, IOE, Tribhuvan university, functional nanomaterial lab kritipur Ktm, and Jeonbuk National University, Republic of Korea.

References

[1] M. A. Rabbani, “Supercapacitor and battery energy storage systems integrated renewable energy sources–A minireview,” *Journal of Energy Storage*, vol. 146, p. 120012, Feb. 2026, doi: 10.1016/j.est.2025.120012.

[2] J. Jiang and J. Liu, “Iron anode-based aqueous electrochemical energy storage devices: Recent advances and future perspectives,” *Interdisciplinary Materials*, vol. 1, no. 1, pp. 116–139, Jan. 2022, doi: 10.1002/idm2.12007.

[3] A. González, E. Goikolea, J. A. Barrena, and R. Mysyk, “Review on supercapacitors: Technologies and materials,” *Renewable and Sustainable Energy Reviews*, vol. 58, pp. 1189–1206, May 2016, doi: 10.1016/j.rser.2015.12.249.

[4] S. Manandhar, S. Shahi, C. L. Gnawali, K. Ariga, and L. K. Shrestha, “Turning biowaste Terminalia bellirica seed into energy: Nanoarchitectonics of hierarchical porous carbon for supercapacitor applications,” *Journal of Power Sources*, vol. 689, p. 240759, Oct. 2026, doi: 10.1016/j.jpowsour.2026.240759.

[5] S. Ahmed, P. Sospiro, M.-S. Gulino, M. Laschi, D. Vangi, and D. Bregoli, “Hybrid Energy Storage Systems as Circular and Sustainable Enablers for Electric Mobility: A Comparative Assessment of Batteries and Supercapacitors,” *Sustainability*, vol. 18, no. 6, p. 2686, Mar. 2026, doi: 10.3390/su18062686.

[6] P. S. Kumar, K. G. Pavithra, and Mu. Naushad, “Characterization techniques for nanomaterials,” in *Nanomaterials for Solar Cell Applications*, Elsevier, 2019, pp. 97–124. doi: 10.1016/B978-0-12-813337-8.00004-7.

[7] C. L. Gnawali *et al.*, “Nanoporous Activated Carbon Material from Terminalia chebula Seed for Supercapacitor Application,” *C*, vol. 9, no. 4, p. 109, Nov. 2023, doi: 10.3390/c9040109.

[8] J. Sun, B. Luo, and H. Li, “A Review on the Conventional Capacitors, Supercapacitors, and Emerging Hybrid Ion Capacitors: Past, Present, and Future,” *Adv Energy and Sustain Res*, vol. 3, no. 6, p. 2100191, Jun. 2022, doi: 10.1002/aesr.202100191.

[9] M. G. Ashritha and K. Hareesh, “Electrode materials for EDLC and pseudocapacitors,” in *Smart Supercapacitors*, Elsevier, 2023, pp. 179–198. doi: 10.1016/B978-0-323-90530-5.00033-2.

[10] O. Stamm, U. Latscha, P. Janecek, and A. Campana, “Development of a special electrode for continuous subcutaneous pH measurement in the infant scalp,” *Am J Obstet Gynecol*, vol. 124, no. 2, pp. 193–195, Jan. 1976, doi: 10.1016/s0002-9378(16)33297-5.

[11] N. Parvin, D. Merum, M. Kang, S. W. Joo, J. H. Jung, and T. K. Mandal, “Recent advances in hybrid supercapacitors: a review of high-performance materials and scalable fabrication techniques,” *J. Mater. Chem. A*, vol. 13, no. 30, pp. 24320–24386, 2025, doi: 10.1039/D5TA02887F.

[12] M. A. Saghafizadeh, A. M. Zardkhoshoui, and S. S. Hosseiny Davarani, “Hybrid supercapacitors with MnTe@ZnMnTe hollow octahedrons encapsulated with reduced graphene oxide for high-performance hybrid supercapacitors,” *Chemical Engineering Journal*, vol. 508, p. 160817, Mar. 2025, doi: 10.1016/j.cej.2025.160817.

[13] M. H. Boratto, J. V. M. Lima, G. G. Malliaras, and C. F. O. Graeff, “Supercapacitor auto analyser: An automated data analysis software for supercapacitor characterization,” *Journal of Energy Storage*, vol. 63, p. 107095, Jul. 2023, doi: 10.1016/j.est.2023.107095.

[14] N. L. Rosi *et al.*, “Hydrogen Storage in Microporous Metal-Organic Frameworks,” *Science*, vol. 300, no. 5622, pp. 1127–1129, May 2003, doi: 10.1126/science.1083440.

[15] C. Huang *et al.*, “A General Synthesis of Nanostructured Conductive Metal–Organic Frameworks from Insulating MOF Precursors for Supercapacitors and Chemiresistive Sensors,” *Angew Chem Int Ed*, vol. 63, no. 3, p. e202313591, Jan. 2024, doi: 10.1002/anie.202313591.

[16] H.-C. Zhou, J. R. Long, and O. M. Yaghi, “Introduction to Metal–Organic Frameworks,” *Chem. Rev.*, vol. 112, no. 2, pp. 673–674, Feb. 2012, doi: 10.1021/cr300014x.

[17] H. Furukawa, K. E. Cordova, M. O’Keeffe, and O. M. Yaghi, “The Chemistry and Applications of Metal-Organic Frameworks,” *Science*, vol. 341, no. 6149, p. 1230444, Aug. 2013, doi: 10.1126/science.1230444.

[18] J. Ding *et al.*, “The synthesis of MOF derived carbon and its application in water treatment,” *Nano Res.*, vol. 15, no. 8, pp. 6793–6818, Aug. 2022, doi: 10.1007/s12274-022-4327-1.

[19] E. G. Rasmussen, J. Kramlich, and I. V. Novosselov, “Synthesis of metal-organic framework HKUST-1 via tunable continuous flow supercritical carbon dioxide reactor,” *Chemical Engineering Journal*, vol. 450, p. 138053, Dec. 2022, doi: 10.1016/j.cej.2022.138053.

[20] X.-C. Xie, K.-J. Huang, and X. Wu, “Metal–organic framework derived hollow materials for electrochemical energy storage,” *J. Mater. Chem. A*, vol. 6, no. 16, pp. 6754–6771, 2018, doi: 10.1039/C8TA00612A.

[21] V. F. Yusuf, N. I. Malek, and S. K. Kailasa, “Review on Metal–Organic Framework Classification, Synthetic Approaches, and Influencing Factors: Applications in Energy,

Drug Delivery, and Wastewater Treatment," *ACS Omega*, vol. 7, no. 49, pp. 44507–44531, Dec. 2022, doi: 10.1021/acsomega.2c05310.

[22] A. Puri, S. Shahi, C. L. Gnawali, K. Ariga, and L. K. Shrestha, "Nanoarchitectonics of Nanoporous Carbon Materials from *Achyranthus bidentata* (Datiwan) Stem for Supercapacitor Applications," *J. Oleo Sci.*, vol. 75, no. 3, pp. 367–378, 2026, doi: 10.5650/jos.ess25269.

[23] Y. Pang, X. Zheng, S. Wu, F. Wang, Z. Shen, and H. Chen, "Bimetallic and multimetallic MOFs and their derivatives," in *Metal Organic Frameworks and Their Derivatives for Energy Conversion and Storage*, Elsevier, 2024, pp. 37–62. doi: 10.1016/B978-0-443-18847-3.00014-6.

[24] K. A. Adegoke and P. F. Tseki, "Trimetallic metal–organic frameworks for CO_2 reduction reactions," *Phys. Chem. Chem. Phys.*, vol. 28, no. 15, pp. 9043–9070, 2026, doi: 10.1039/D5CP04062K.

[25] Y. Li *et al.*, "Synthesis and shaping of metal–organic frameworks: a review," *Chem. Commun.*, vol. 58, no. 82, pp. 11488–11506, 2022, doi: 10.1039/D2CC04190A.

[26] C.-W. Huang, V.-H. Nguyen, S.-R. Zhou, S.-Y. Hsu, J.-X. Tan, and K. C.-W. Wu, "Metal–organic frameworks: preparation and applications in highly efficient heterogeneous photocatalysis," *Sustainable Energy Fuels*, vol. 4, no. 2, pp. 504–521, 2020, doi: 10.1039/C9SE00972H.

[27] Y.-R. Lee, J. Kim, and W.-S. Ahn, "Synthesis of metal-organic frameworks: A mini review," *Korean J. Chem. Eng.*, vol. 30, no. 9, pp. 1667–1680, Sep. 2013, doi: 10.1007/s11814-013-0140-6.

[28] J. Bedia, V. Muelas-Ramos, M. Peñas-Garzón, A. Gómez-Avilés, J. Rodríguez, and C. Belver, "A Review on the Synthesis and Characterization of Metal Organic Frameworks for Photocatalytic Water Purification," *Catalysts*, vol. 9, no. 1, p. 52, Jan. 2019, doi: 10.3390/catal9010052.

[29] J. H. Bang and K. S. Suslick, "Applications of Ultrasound to the Synthesis of Nanostructured Materials," *Advanced Materials*, vol. 22, no. 10, pp. 1039–1059, Mar. 2010, doi: 10.1002/adma.200904093.

[30] S. Soni, P. K. Bajpai, and C. Arora, "A review on metal-organic framework: Synthesis, properties and ap-plication," *CAN*, vol. 3, no. 2, p. 87, Sep. 2020, doi: 10.24294/can.v3i2.551.

[31] S. Q. Zheng *et al.*, "Solvothermal synthesis of nanostructured nickel-based metal–organic frameworks (Ni-MOFs) with enhanced electrochemical performance for symmetric supercapacitors," *J Mater Sci*, vol. 58, no. 29, pp. 11894–11913, Aug. 2023, doi: 10.1007/s10853-023-08747-2.

[32] A. A. Bhoite, V. A. Sawant, and N. L. Tarwal, "Solvothermal synthesis of Ni/Co-based metal-organic framework with nanosheets-like structure for high-performance supercapacitor," *Colloids and Surfaces A: Physicochemical and Engineering Aspects*, vol. 702, p. 134814, Dec. 2024, doi: 10.1016/j.colsurfa.2024.134814.

[33] A. Paul, A. Karmakar, and A. J. L. Pombeiro, "Aspects of Hydrothermal and Solvothermal Methods in MOF Chemistry," 2024, pp. 281–312. doi: 10.1142/9789811283208_0009.

[34] Z. Hu, Y. Wang, and D. Zhao, "Modulated Hydrothermal Chemistry of Metal–Organic Frameworks," *Acc. Mater. Res.*, vol. 3, no. 11, pp. 1106–1114, Nov. 2022, doi: 10.1021/accountsmr.2c00104.

[35] D. K. Singha, R. I. Mohanty, P. Bhanja, and B. K. Jena, "Metal–organic framework and graphene composites: advanced materials for electrochemical supercapacitor applications," *Mater. Adv.*, vol. 4, no. 20, pp. 4679–4706, 2023, doi: 10.1039/D3MA00523B.

[36] A. U. Rehman *et al.*, "MOF-Based Composite Materials for Supercapacitors: Design, Performance, and Challenges," *Chemistry – An Asian Journal*, vol. 20, no. 17, p. e00453, Sep. 2025, doi: 10.1002/asia.202500453.

[37] H. B. Albargi *et al.*, "'Advanced hierarchical MIL-53/Ti3C2@MnO2 composites for superior supercapattery performance and efficient hydrogen evolution reaction,'" *Diamond and Related Materials*, vol. 156, p. 112409, Jun. 2025, doi: 10.1016/j.diamond.2025.112409.

[38] X. Zhang and Y. Ding, "Research Progress on the Application of MOF Materials in Lithium-Ion Batteries," *Battery Energy*, vol. 4, no. 1, p. 20240046, Jan. 2025, doi: 10.1002/bte2.20240046.

[39] C. Zhou *et al.*, "Self-supporting electrode engineering design with composite conductive network for asymmetric MnO2//AC supercapacitor," *Sustainable Materials and Technologies*, vol. 40, p. e00891, Jul. 2024, doi: 10.1016/j.susmat.2024.e00891.

[40] H. Ze *et al.*, "Deciphering the Competitive Charge Storage Chemistry of Metal Cations and Protons in Aqueous MnO_2 -Based Supercapacitors," *J. Am. Chem. Soc.*, vol. 147, no. 11, pp. 9620–9628, Mar. 2025, doi: 10.1021/jacs.4c17458.

[41] C. Yuan, H. B. Wu, Y. Xie, and X. W. (David) Lou, "Mixed Transition-Metal Oxides: Design, Synthesis, and Energy-Related Applications," *Angew Chem Int Ed*, vol. 53, no. 6, pp. 1488–1504, Feb. 2014, doi: 10.1002/anie.201303971.

[42] F. He *et al.*, "Hydrothermal synthesis of Ni-based metal organic frameworks/graphene oxide composites as supercapacitor electrode materials," *J. Mater. Res.*, vol. 35, no. 11, pp. 1439–1450, Jun. 2020, doi: 10.1557/jmr.2020.93.

[43] L. Gao, F. Liu, J. Qi, W. Gao, and G. Xu, "Recent Advances and Challenges in Hybrid Supercapacitors Based on Metal Oxides and Carbons," *Inorganics*, vol. 13, no. 2, p. 49, Feb. 2025, doi: 10.3390/inorganics13020049.

[44] B. Li, H. Wen, Y. Cui, W. Zhou, G. Qian, and B. Chen, "Emerging Multifunctional Metal–Organic Framework Materials," *Advanced Materials*, vol. 28, no. 40, pp. 8819–8860, Oct. 2016, doi: 10.1002/adma.201601133.

[45] Y. Wang, T. Xu, K. Liu, M. Zhang, X. Cai, and C. Si, "Biomass-based materials for advanced supercapacitor: principles, progress, and perspectives," *Aggregate*, vol. 5, no. 1, p. e428, Feb. 2024, doi: 10.1002/agt2.428.

[46] R. Bhosale, S. Bhosale, D. Narale, C. Jambhale, and S. Kolekar, "Construction of Well-Defined Two-Dimensional Architectures of Trimetallic Metal–Organic Frameworks for High-Performance Symmetric Supercapacitors," *Langmuir*, vol. 39, no. 34, pp. 12075–12089, Aug. 2023, doi: 10.1021/acs.langmuir.3c01337.

[47] M. Sethi, U. S. Shenoy, and D. K. Bhat, "A porous graphene–$NiFe_2O_4$ nanocomposite with high electrochemical performance and high cycling stability for energy storage

applications," *Nanoscale Adv.*, vol. 2, no. 9, pp. 4229–4241, 2020, doi: 10.1039/D0NA00440E.

[48] W. Dong, M. Xie, S. Zhao, Q. Qin, and F. Huang, "Materials design and preparation for high energy density and high power density electrochemical supercapacitors," *Materials Science and Engineering: R: Reports*, vol. 152, p. 100713, Feb. 2023, doi: 10.1016/j.mser.2022.100713.

[49] T. Mukhiya *et al.*, "Engineering nanohaired 3D cobalt hydroxide wheels in electrospun carbon nanofibers for high-performance supercapacitors," *Chemical Engineering Journal*, vol. 361, pp. 1225–1234, Apr. 2019, doi: 10.1016/j.cej.2019.01.006.

[50] K. Chhetri *et al.*, "Controlled Selenium Infiltration of Cobalt Phosphide Nanostructure Arrays from a Two-Dimensional Cobalt Metal–Organic Framework: A Self-Supported Electrode for Flexible Quasi-Solid-State Asymmetric Supercapacitors," *ACS Appl. Energy Mater.*, vol. 4, no. 1, pp. 404–415, Jan. 2021, doi: 10.1021/acsaem.0c02340.

[51] C. F. Holder and R. E. Schaak, "Tutorial on Powder X-ray Diffraction for Characterizing Nanoscale Materials," *ACS Nano*, vol. 13, no. 7, pp. 7359–7365, Jul. 2019, doi: 10.1021/acsnano.9b05157.

[52] N. I. Prasianakis, "AI-enhanced X-ray diffraction analysis: towards real-time mineral phase identification and quantification," *IUCrJ*, vol. 11, no. 5, pp. 647–648, Sep. 2024, doi: 10.1107/S2052252524008157.

[53] Y. S. Choudhary, L. Jothi, and G. Nageswaran, "Electrochemical Characterization," in *Spectroscopic Methods for Nanomaterials Characterization*, Elsevier, 2017, pp. 19–54. doi: 10.1016/B978-0-323-46140-5.00002-9.

[54] F. Marken, A. Neudeck, and A. M. Bond, "Cyclic Voltammetry," in *Electroanalytical Methods*, F. Scholz, A. M. Bond, R. G. Compton, D. A. Fiedler, G. Inzelt, H. Kahlert, Š. Komorsky-Lovrić, H. Lohse, M. Lovrić, F. Marken, A. Neudeck, U. Retter, F. Scholz, and Z. Stojek, Eds., Berlin, Heidelberg: Springer Berlin Heidelberg, 2010, pp. 57–106. doi: 10.1007/978-3-642-02915-8_4.

[55] S. A. Bhat, V. Kumar, S. Kumar, A. E. Atabani, I. Anjum Badruddin, and K.-J. Chae, "Supercapacitors production from waste: A new window for sustainable energy and waste management," *Fuel*, vol. 337, p. 127125, Apr. 2023, doi: 10.1016/j.fuel.2022.127125.

[56] S. Rodrigues, A. K. Shukla, and N. Munichandraiah, "A cyclic voltammetric study of the kinetics andmechanism of electrodeposition of manganese dioxide," *Journal of Applied Electrochemistry*, vol. 28, no. 11, pp. 1235–1241, Nov. 1998, doi: 10.1023/A:1003472901760.

[57] S. Ayman, A.-H. Sakr, S. Ebrahim, M. Soliman, A. M. Elshaer, and Y. Elkony, "Binary nanocomposite of polyindole intercalated with nickel cobaltite as high-performance supercapacitor electrode," *Materials Chemistry and Physics*, vol. 332, p. 130270, Feb. 2025, doi: 10.1016/j.matchemphys.2024.130270.

[58] C. Pan, B. Li, H. Yin, X. He, and Y. Gao, "Nickel-rich ternary cathode material as a novel capping layer to improve lithium iron phosphate electrochemical performance," *Electrochimica Acta*, vol. 496, p. 144421, Aug. 2024, doi: 10.1016/j.electacta.2024.144421.

[59] A. A. Moya, “A physically consistent electric circuit to interpret the galvanostatic charge-discharge curves of electric double layer capacitors,” *Journal of Power Sources*, vol. 656, p. 238050, Nov. 2025, doi: 10.1016/j.jpowsour.2025.238050.

[60] F. Licht, M. A. Davis, and H. A. Andreas, “Charge redistribution and electrode history impact galvanostatic charging/discharging and associated figures of merit,” *Journal of Power Sources*, vol. 446, p. 227354, Jan. 2020, doi: 10.1016/j.jpowsour.2019.227354.

[61] R. R. Salunkhe *et al.*, “Chemical synthesis and electrochemical analysis of nickel cobaltite nanostructures for supercapacitor applications,” *Journal of Alloys and Compounds*, vol. 509, no. 23, pp. 6677–6682, Jun. 2011, doi: 10.1016/j.jallcom.2011.03.136.